GAS COMPOSITION STUDIES AT THE 2015 ATLAS TRT TEST BEAM

by

Emre Çelebi

B.S., Physics, Boğaziçi University, 2012

Submitted to the Institute for Graduate Studies in
Science and Engineering in partial fulfillment of
the requirements for the degree of
Master of Science

Graduate Program in Physics
Boğaziçi University
2016

ACKNOWLEDGEMENTS

I would like to thank my supervisors Erkcan Özcan and Serkant Ali Çetin for supporting me, for giving me this opportunity and inspiring me in nearly every talk we had. I also thank Gökhan Ünel for him being a motivating element for people around him like me.

I would also like to thank Anatoli Romaniouk, without whose help I would simply be lost, and Viladimir Tikhamirov for his insights and careful explanations.

I want to express my gratitude to İsmail Okan Atakişi and Eda Yıldırım for their uplifting conversations, to Saime Gürbüz for constantly reminding the work and Şahin Taşın for his pep talks.

I can't thank enough to my family, especially my parents Mevlidiye Çelebi, Hayrullah Çelebi and my sister Elif Çelebi for their patience, support and love.

I would like thank to my girlfriend Şüheda Demir for her care, understanding and the light she brings to my life.

Lastly, I would like to thank everybody in the Engin Arık High Energy Physics Laboratory; they are the perfect team to nourish ideas and a second family that one can count on.

ABSTRACT

GAS COMPOSITION STUDIES AT THE 2015 ATLAS TRT TEST BEAM

Transition Radiation Tracker (TRT) is a subsystem of the ATLAS inner detector. It provides many hits on charged particle tracking and helps particle identification by measuring transition radiation. At the end of the first run of the Large Hadron Collider, TRT has suffered from some unforeseen effects where caused miniature cracks in its gas pipes. These resulted in gas leaks at a level where using the usual Xenon based gas mixture was no longer feasible in certain parts of the detector.

In an effort to understand the transition radiation photon capture performance of the substitute gas mixtures, Krypton-based and Argon-based mixtures, test beam studies using a smaller transition radiation detector (TRD) were undertaken during 2015.

In this thesis, we present; this test detector, the relevant test-beam setup, the calibration of the system, the analysis of the data and the results in the form of probability-to-exceed-threshold plots; which can be used as input to future detailed Monte Carlo simulations that are needed to define optimal TRT operating points with substitute gas mixtures. Our results verified that the transition radiation performance of the Krypton gas mixture is better than the Argon mixture but is outperformed by the original Xenon mixture.

ÖZET

2015 ATLAS TRT TEST BEAM'DE GAZ KARIŞIMI ÇALIŞMALARI

Transition Radiation Tracker (TRT, geçiş ışıması iz sürücüsü) ATLAS algıcının iç algıç kısmının bir alt sistemidir. Yüklü parçacıkların izlerinin sürmülmesinde kullanılmak üzere pek çok ölçüm sağlamasının yanında, parçacık tanımaya geçiş ışınımı ölçümü yaparak katkıda bulunur. Büyük Hadron Çarpıştırıcısı'nın (Large Hadron Collider) birinci çalışma döneminin sonunda, önceden öngörülemeyen etkilerden dolayı TRT gaz borularında çatlaklar oluşmuştur. Çatlakların yarattığı gaz kaçağı, algıcın belirli bölgelerinde Ksenon temelli gaz karışımının kullanılmasını ekonomik olmaktan çıkarmıştır.

Temel gaz karışımının yerine kullanılabilecek olan (Kripton ve Argon temelli) gaz karışımlarının geçiş ışınımı fotonlarını yakalama performansının anlaşılması için küçük bir geçiş ışınımı algıcının yardımı ile test demetiyle çalışmalar 2015 yılında gerçekleştirilmiştir.

Bu tez dahilinde sunduklarımız şöyle sıralanabilir; kullanilan test algıcı, test demeti sisteminin kurgusu, sistemin ölçümler için ayarlanması (kalibrasyon), verilerin analizi ve bulguların eşik geçme ihtimali çizimleri şeklinde gösterimi. En sonda sunduğumuz bu çizimler gelecekte yapılacak detaylı bir Monte Carlo benzetimine girdi olarak kullanılacaktır ve böylelikle benzetim, bahsi geçen gaz karışımlarında TRT'nin en uygun çalışma noktasının bulunmasında kullanılabilir hale gelecektir. Bulgularımız, Kripton temelli gaz karışımının geçiş ışınımını ölçme performansının argon temelli olandan daha yüksek olduğunu, ancak Ksenon temelli karışımın performansına ulaşamadığını doğrulamaktadır.

TABLE OF CONTENTS

LIST OF FIGURES

LIST OF SYMBOLS

A	Atomic weight of the absorbing material
c	Speed of light
C	Shell correction
e^-	Electron
I	Mean excitation potential
m_e	Electron mass
N_a	Avagadro's number
P_{e^-}	Probability-to-exceed-threshold for electrons
P_{π^-}	Probability-to-exceed-threshold for pions
π^-	Pion
r_e	Classical electron radius
v	Speed of the particle
W_{max}	Maximum energy transfer in a single collision
z	Charge of incident particle in units of e
Z	Atomic number of absorbing material
β	v/c of the incident particle
γ	Lorentz factor
δ	Density correction term
η	Pseudo-rapidity
θ	Polar Angle
ρ	Density of absorbing material

LIST OF ACRONYMS/ABBREVIATIONS

ALICE	A Large Ion Collider Experiment
ASDBLR	Amplifier/Shaper/Discriminator with Baseline Restoration
ATLAS	A Toroidal LHC Apparatus
BES-III	Beijing Spectrometer - III
BL4S	Beamline for schools
CERN	European Organization for Nuclear Research
CMS	Compact Muon Solenoid
CSC	Cathode Strip Chambers
DTMROC	Drift Time Measurement Readout Chip
FCal	Forward Calorimeter
GUI	Graphical User Interface
HLT	High Level Trigger
HL	High-level
HT	High-level threshold
IBL	Insertable B-Layer
LAr	Liquid Argon
LHC	Large Hadron Collider
LHC-b	Large Hadron Collider beauty experiment
L1	Level 1
LT	Low-level threshold
MDT	Monitored Drift Tubes
NTP	Normal Temperature and Pressure
OHP	Online Histogram Presenter
PID	Particle Identification
QDC	Charge to Digital Converter
RPC	Restive Plate Chamber
ROI	Region of Interest
SCT	Semiconductor Tracker

SM	Standard Model
SPS	Super Proton Synchrotron
SUSY	Supersymmetry
TDC	Time to Digital Converter
TGC	Thin Gap Chamber
TR	Transition Radiation
TRD	Transiton Radiation Detector
TRT	Transition Radiation Tracker

1. INTRODUCTION

At the end of the 19th century, radiation from various sources was observed employing metastable media such as photographic films.

In the early 20th century the technology to detect subatomic particles started to get developed by the invention of ways to measure the ionization caused by radiation in gases. This involved amplification by inducing ion-electron avalanches in gases and measuring them using electrical equipment. Soon enough even the signals from a single ionization event became accessible.

Starting with the 1960s, capabilities of the gaseous detectors extended in to tracking of the particle ionization trails as well. Since then, as gaseous detectors came to present an affordable way for tracking in large volumes, they became an integral part of many large high energy experiments, such as the currently running ALICE at CERN and BES-III at IHEP. One such gaseous detector, named the Transition Radiation Tracker (TRT), is being used in the ATLAS Detector, which is studying collisions at the Large Hadron Collider. TRT measurements provide data not only for tracking but also for particle identification (PID).

In this thesis, we present a test beam study aiming to assess the effects of changing the gas composition in the TRT and the transition radiation analysis performed on the collected data.

2. CERN, LHC, AND THE ATLAS EXPERIMENT

2.1. CERN and LHC

CERN (European Organization for Nuclear Research) is a multinational research laboratory founded in 1954. CERN houses the largest particle accelerator in the world, the Large Hadron Collider (LHC). LHC consists of 1232 super conductor bending magnets, 392 quadrupole focusing magnets and accelerating structures. It is inside a 27 km circular tunnel located on France-Switzerland border. Two beams of particles are accelerated and circulated in opposite directions on the LHC ring. Particle beams collide at 4 detector locations, where the big experiments; ALICE, ATLAS, CMS and LHC-b are stationed around each interaction point (Figure 2.1).

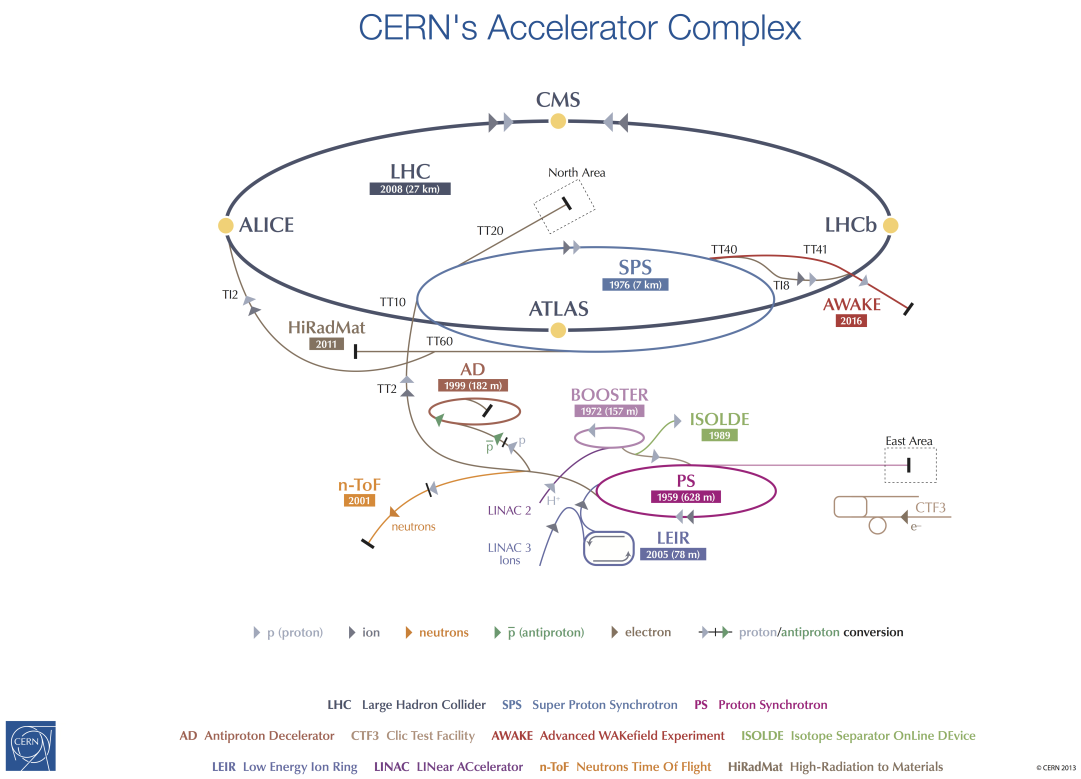

Figure 2.1. The CERN accelerator complex [1].

2.2. ATLAS

The ATLAS detector is designed to study a wide range of physics topics like the Standard Model (SM) and beyond SM searches like SUSY, dark matter etc. It provides full solid angle coverage around the interaction point as much as possible so that the majority of the particles produced in these collisions can have a chance to be detected.

Detector is about 46m long and 25m tall, weighing about 7000 tons. It is located in a cavern 100m below ground.

ATLAS has a layered structure, with each layer of the detector fulfilling a different and complementary purpose. Detector layers can roughly be studied under three sub groups: the Inner Detector, the Calorimeter and the Muon Spectrometer. Together with the Magnet System, Detector systems and the Trigger and Data Acquisition System (TDAQ) constitute major components of ATLAS.

2.2.1. ATLAS Coordinates

ATLAS coordinate system is a right-handed coordinate system with its origin at the interaction point. The z axis lies along the beam axis, the x axis points to center of the LHC ring and the y axis is perpendicular to plane that the LHC ring lies on and points upwards.

Since the detector has been designed to be rotationally symmetric around the z axis, spherical coordinates (r, θ, ϕ) become useful. r denotes distance from interaction point, ϕ denotes the azimuthal angle in the x-y plane and θ is the angle with respect to the z axis.

Since differences in rapidity is a Lorentz-invariant quantity that allows more meaningful ways to measure angular distance between relativistic particles, pseudo-rapidity η is often used.

$$\eta = -\ln\left(\tan\left(\frac{\theta}{2}\right)\right) \tag{2.1}$$

2.2.2. The Inner Detector

Inner detector is the innermost part of the detector. It measures passage of particles with fine granularity, with the purpose of extracting their trajectories. The whole inner detector is situated inside of a solenoid magnet, which means the particles are subjected to ∼2 Tesla magnetic field parallel to the beam axis. Trajectory of the particle in the magnetic field allows the measurement of the momentum over charge value. The inner detector has three subsystems namely the PIXEL, Semiconductor Tracker (SCT) and the Transition Radiation Tracker (TRT) (see Figure 2.2).

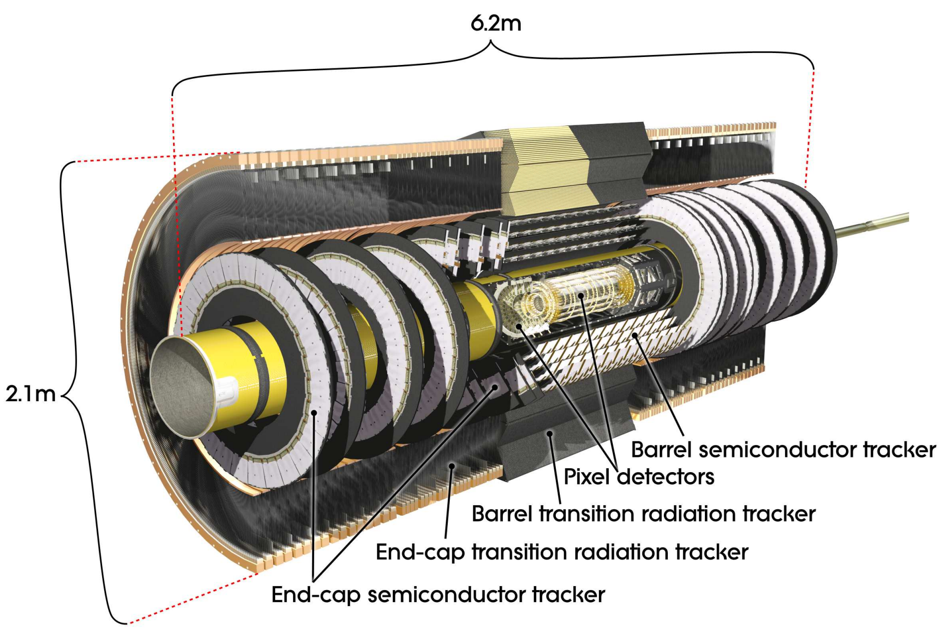

Figure 2.2. Inner detector and its components [2].

2.2.2.1. PIXEL. Counting its new layer, the Insertable B-Layer (IBL), which was installed in 2014, the PIXEL is organized in to four cylindrical layers in the center (barrel), and 3 disks on two sides (endcaps). PIXEL has roughly 92 million channels (including the IBL channels).

PIXEL detector has an intrinsic resolution of 10 μm in R-ϕ and 115 μm in z and the IBL has 8 μm in R-ϕ and 40 μm in z. It covers $|\eta|<2.5$. The innermost layer (IBL) is located at a radius of 33.3 mm. The outermost barrel layer is located at a radius of 122.5 mm. [13]

2.2.2.2. SCT. Semiconductor Tracker (SCT) has a total of 6.3 million channels. In general SCT provides 4 space points for tracking. In the barrel region it has 4 layers and in the endcap region 9 disk shaped layers in each end cap region. It has a spatial resolution of 17 μm in R-ϕ and 580 μm in z (in R for endcap disks). [13]

2.2.2.3. TRT. TRT is the outermost part of the inner detector. It is a gaseous ionization detector consisting of ~300000 small diameter proportional counters called straws. TRT has ~130 μm drift radius resolution but it does not provide position measurement along the drift tube. Along with the tracking ability, TRT helps particle identification by measuring transition radiation on the path. More details about the TRT will be provided in Chapter 4.

2.2.3. The Calorimeter System

There are two calorimeter subsystems in ATLAS namely electromagnetic and hadronic (Figure 2.3). Their job is to measure energy of the particles. They stop majority of the particles, only muons, neutrinos and some hypothetical particles like the lightest supersymmetric particles escape outside.

2.2.3.1. The Electromagnetic Calorimeter. In the electromagnetic calorimeter, lead is used as sampling material and liquid argon is the active material. Lead sheets have two 0.2 mm thick steel sheets glued to them and the lead sheet thickness varies between 1.13 mm and 2.2 mm in different η regions in the barrel and endcap. [2] Electrodes and absorbers are shaped in an accordion-like geometry in order to have

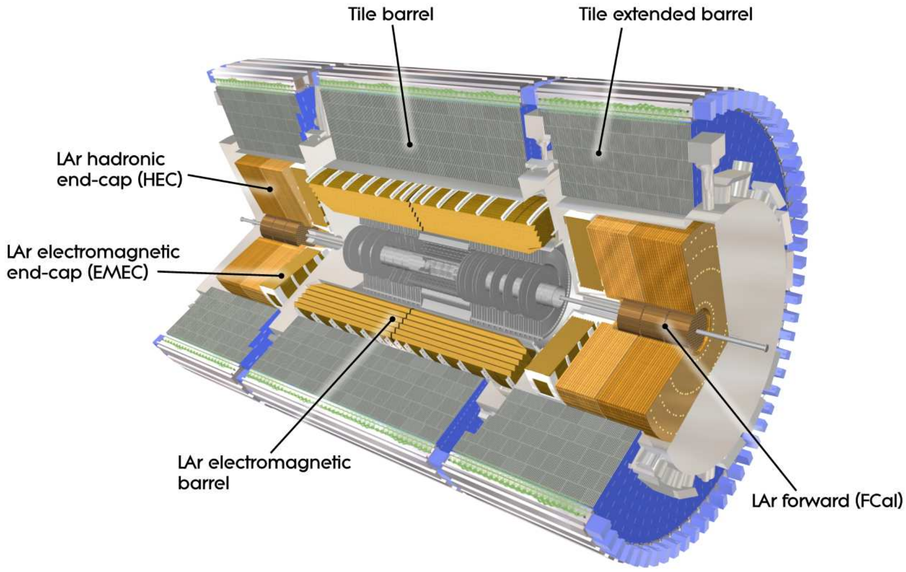

Figure 2.3. Atlas Calorimeter [2].

uniform performance in ϕ. In the barrel bending angles and wave amplitudes are such that the gap between electrode and the absorber is constant. The barrel covers $|\eta|<1.475$ and the endcaps cover $1.375<|\eta|<3.2$.

2.2.3.2. The Hadronic Calorimeter. Hadronic calorimeter is situated outside of the electromagnetic calorimeter. Different technology is used for different η regions; Tile Calorimeter (TileCal), LAr Hadronic Endcap Calorimeter, Forward Calorimeters. TileCal barrel covers the region $|\eta|<1.0$ and two extended TileCal barrels covers the region $0.8<|\eta|<1.7$. Absorbers of TileCal are steel and scintillator tiles detect the shower. The LAr Hadronic Endcap Calorimeter is placed right after the LAr Electromagnetic Calorimeter. It covers the region $1.5<|\eta|<3.2$. Copper plates are the absorber material and the liquid argon is used as detecting material. The Forward Calorimeters (FCal) cover the region $3.1<|\eta|<4.9$. FCal has three modules, one made with copper other two with tungsten.

2.2.4. The Muon Spectrometer and The Toroid Magnets

ATLAS uses aircore superconducting toroid magnets to bend muon path so that the muon spectrometer can measure their momenta. There are two endcap and one barrel toroid magnets and their joint magnetic field is mostly perpendicular to the trajectory. Bending power is between 1.5 and 5.5 Tm in range $0<|\eta|<1.4$,between 1 and 7.5 Tm in range $1.6<|\eta|<2.7$ [2].

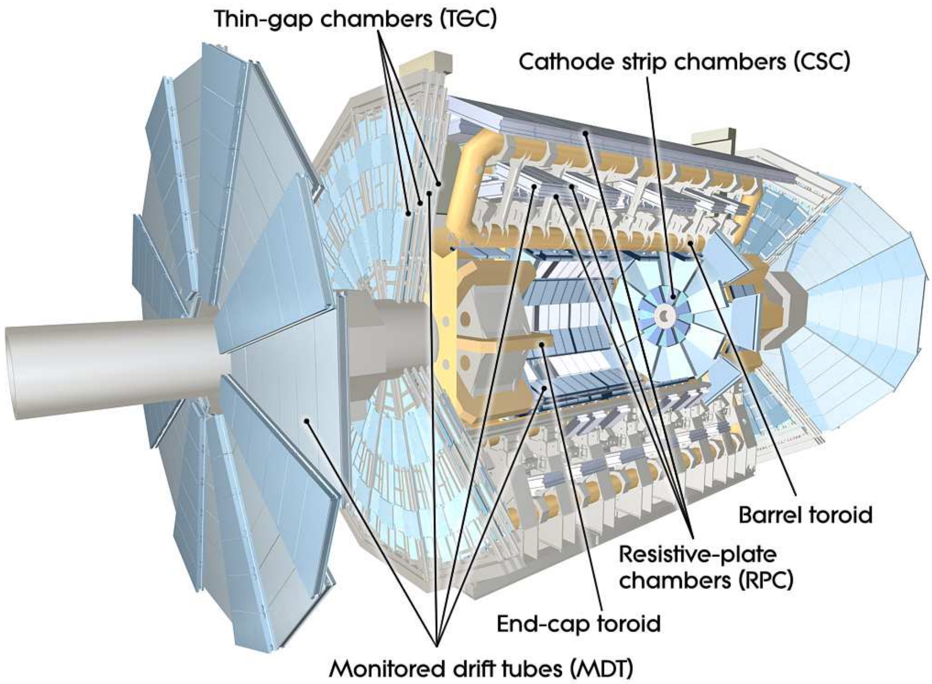

Figure 2.4. ATLAS Muon Spectrometer and the toroid magnets [2].

The muon spectrometer components (Figure 2.4) can be listed as; Monitored drift tubes (MDT) for $|\eta|<2.7$, Cathode strip chambers (CSC) for $2.0<|\eta|<2.7$, Resistive plate chambers (RPC) for $|\eta|<1.05$ and Thin gap chambers (TGC) for $1.05<|\eta|<2.7$. MDT and CSC are used for precision tracking, whereas RPC and TGC are used for triggering and for obtaining additional tracking data.

2.2.5. The Trigger and Data Acquisition (TDAQ)

ATLAS, being an LHC experiment, has to process large amount of events. It is nearly impossible to obtain data from all events for multiple reasons like dead time of the detectors, maximum available disk space, etc. Therefore trigger is used to reduce uninteresting data. Overall, the trigger rate of ATLAS is around a couple of hundred Hz, while LHC bunch crossing rate is 40 MHz.

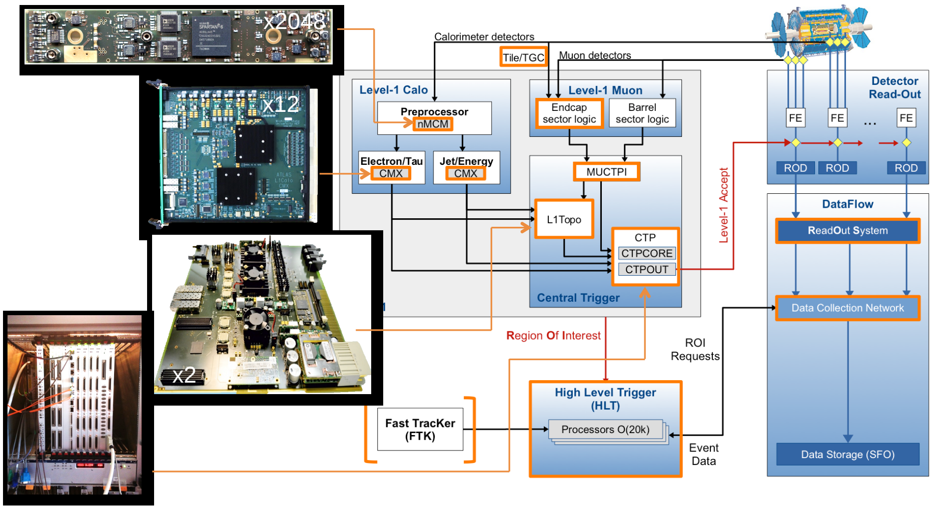

Figure 2.5. TDAQ workflow in LHC Run 2 [3].

The first level trigger (L1) is a hardware trigger. L1 selects events if there are hints of valuable data based on crude calculations based on input from the calorimeters and the muon system. Triggered L1 determines ROIs (Region of Interest) and passes them to the High Level trigger (HLT). HLT is software based and performs more detailed analysis using data from all the detector subsystems. Only events selected by the HLT are stored in the data storage [3].

3. GASEOUS PARTICLE DETECTORS AND PROPORTIONAL COUNTERS

3.1. Origins of Gas Detectors

Joseph John Thomson and Ernest Rutherford hypothesized that x-rays ionizes air by stripping negatively charged particles (1896) and then they recognized that recombination could be prevented by applying an electric field. Their following work led to the development of the first gaseous ionization chamber.

John Sealy Townsend's study on charge multiplication in gases and with Hans Geiger's help Rutherford built the first proportional counter in which collected signal changes proportionally to primary ionization (1908) [14]. This detector was using a dedicated gas mixture unlike the first counter that uses air. It was capable of amplifying the primary ionization to a level at which the output was measurable with a simple electroscope.

3.2. Charged Particle Interactions with Matter

An energetic charged particle can loose a portion of its energy due to interaction with the medium it transverses and the trajectory if the particle can deflect. The interaction can be studied under two categories; heavy particles (pion, proton, etc.) and light particles (electrons and positrons).

3.2.1. Heavy Charged Particles

Heavy charged particles like pions interact with the matter mainly through collisions. These collisions are inelastic collisions with atomic electrons and elastic with nuclei. Inelastic collisions are particularly important in the particle detectors since under the right conditions lost energy can pave the way for measurable macroscopic changes.

We may examine inelastic collisions in two groups, namely soft and hard collisions. Soft collisions are inelastic collisions that can cause only excitations. Ionizing collisions are hard collisions since deposited energy with a single interaction can be large compared to excitations. Ionization occurs when an atomic electron receives more energy than its binding energy and as a result escapes from the atom. In the process electron gains energy equal to received energy minus the binding energy. If the resulting electron is energetic enough to produce further ionizations those electrons are called δ-rays or knock-on electrons.

In general the mass of the atom is large hence the energy lost with elastic scattering from the nuclei is small; therefore major loss mechanism is atomic electron collisions. While these collisions are statistical in nature, their number is high and average energy loss does not fluctuate much. Because of this, one can work with average energy loss per length dE/dx.

This value was first calculated by Bohr using classical mechanics and the resulting expression was reasonable to explain heavy particles like α particles,as well as some lighter particles. Later on Bethe formula (equation 3.1) was derived and corrected using quantum mechanics by multiple scientists. Two important corrections to the Bethe formula are density and shell corrections. After those two corrections are applied, the corrected Bethe formula is sufficient for modelling the energy loss by elementary particles (other than electron and positrons).

$$\left\langle \frac{dE}{dx} \right\rangle = 2\pi N_a {r_e}^2 m_e c^2 \rho \frac{Z}{A} \frac{z^2}{\beta^2} \left[\ln\left(\frac{2 m_e v^2 W_{max}}{I^2} \right) - 2\beta^2 - \delta - 2\frac{C}{Z} \right] \tag{3.1}$$

with $2\pi N_a {r_e}^2 m_e c^2 = 0.1535 MeV cm^2/g$,

r_e: classical electron radius $= 2.817 \times 10^{-13}$cm

m_e: electron mass

v: speed of incident particle

C: shell correction

I: mean excitation potential

ρ: density of absorbing material

δ: density correction

N_a: Avagadro's number $= 6.022 \times 10^{23}$ mol^{-1}

z:charge of incident particle in units of e

$\beta = v/c$ of incident particle

$\gamma = 1/\sqrt{1-\beta^2}$

Z: atomic number of absorbing material

A: atomic weight of absorbing material

W_{max}: maximum energy transfer in a single collision

At low energies where the electron orbital velocities for atomic electrons are comparable to incident particle velocity, the assumption of stationary atomic electrons is no longer correct [15]. The so called shell correction term is a correction for the low energy part and it is represented with C in the formula.

When the incident particle speed is high enough, the material it traverses can become polarized. This polarization reduces the interaction range, therefore it reduces the total energy loss. Polarization itself depends on density therefore this term is called as density correction. The density correction term is the δ term in the formula. It is usually computed with Sternheimer's parameterization.

W_{max} (maximum energy transfer) corresponds to the head-on collision case, and is given by:

$$W_{max} = \frac{2m_e c^2 \xi^2}{1 + 2s\sqrt{1+\xi^2} + s^2}$$

where $s = m_e/M$ and $\xi = \beta\gamma$.

I (Mean Excitation Potential) value depends on Z in a complicated manner and the following semi empirical calculations can be used in the absence of tabulated experimental values [15]:

$I/Z = 12 + 7/Z$ if Z <13 and $I/Z = 9.76 + 58.8Z^{-1.19}$ for the rest.

The loss per length as computed with the Bethe formula and various corrections are presented in Figure 3.1.

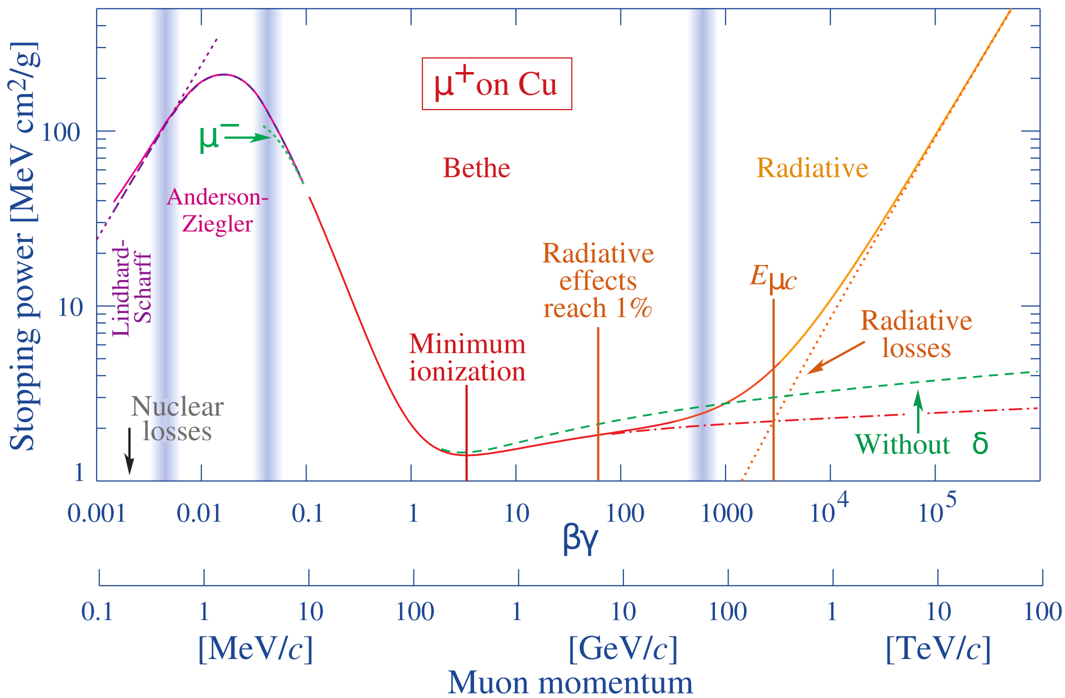

Figure 3.1. Bethe formula and corrections [4].

3.2.2. Interactions of Electrons and Positrons with Matter

In the case of electrons and positrons, the incident particle and the atomic electrons have the same mass and the interaction with matter differs from the interactions of particles like pion or kaon. The mean energy loss is treated as a composition of collision and radiative losses.

$$\frac{dE}{dx}_{tot} = \frac{dE}{dx}_{rad} + \frac{dE}{dx}_{coll} \tag{3.2}$$

The mechanism of collision loss has similar loss processes as the heavy charged particles but their small mass brakes one assumption particularly: in the derivation of the Bethe formula, the incident particle is assumed to be passing without any deflection but this only holds if the particle in hand is heavier than electron.

Moreover, in the electron case, after the collision incident electron can not be distinguished since the two interacting particles are identical. Therefore there are two formulas, for electron and positron separately.

In the electron and atomic-electron collisions, the large energy transfers are described with the Møller cross-section. The maximum energy transfer (W_{max}) is the entire kinetic energy yet we cannot distinguish the incident electron after the collision so maximum energy transfer is taken as the $W_{max}/2$. Equation 3.3 is the dE/dx formula calculated by using the first moment of the Møller cross-section [4].

$$\left\langle \frac{dE}{dx} \right\rangle = 2\pi N_a {r_e}^2 m_e c^2 \rho \frac{Z}{A} \frac{1}{\beta^2} \left[\ln \left(\frac{2m_e \gamma^2 v^2 \{m_e c^2 (\gamma - 1)/2\}}{I^2} \right) + (1 - \beta^2) \right. \\ \left. - \frac{2\gamma - 1}{\gamma^2} \ln 2 + \frac{1}{8} \left(\frac{\gamma - 1}{\gamma} \right)^2 - \delta \right]. \tag{3.3}$$

The positron and atomic electron collisions are described by the Bhabha cross-section. Since the particles are not identical, the maximum energy transfer is the $W_{max} = m_e c^2 (\gamma - 1)$. Equation 3.4 is the dE/dx formula calculated by using the first moment of the Bhabha cross-section [4].

$$\left\langle \frac{dE}{dx} \right\rangle = 2\pi N_a {r_e}^2 m_e c^2 \rho \frac{Z}{A} \frac{1}{\beta^2} \left[\ln \left(\frac{2m_e \gamma^2 v^2 \{m_e c^2 (\gamma - 1)\}}{2I^2} \right) + \ln(1 - \beta^2) \right. \\ \left. - \frac{\beta^2}{12} \left(23 + \frac{14}{\gamma + 1} + \frac{10}{(\gamma + 1)^2} + \frac{4}{(\gamma + 1)^3} \right) - \delta \right]. \tag{3.4}$$

When an electron or positron is accelerated on the electric field of the nucleus it it emits a real photon. This photon energy is equal to the lost energy of the incident particle. The dominant effect at high energy electrons and positrons is the energy loss by radiation, mainly Bremsstrahlung. It only becomes relevant for heavy particles after a few hundred GeV energies.

Bremsstrahlung losses are almost linearly increasing with the incident particle energy and it surpasses the collision loss after the so called critical energy. ($\frac{dE}{dx}_{rad} = \frac{dE}{dx}_{coll}$ for $E = E_c$).

Figure 3.2 shows $dE/dx{\times}X_0$ where X_0 is the radiation length i.e. the mean distance required to reduce the electron energy to $1/e$ of its original value by radiative losses only.

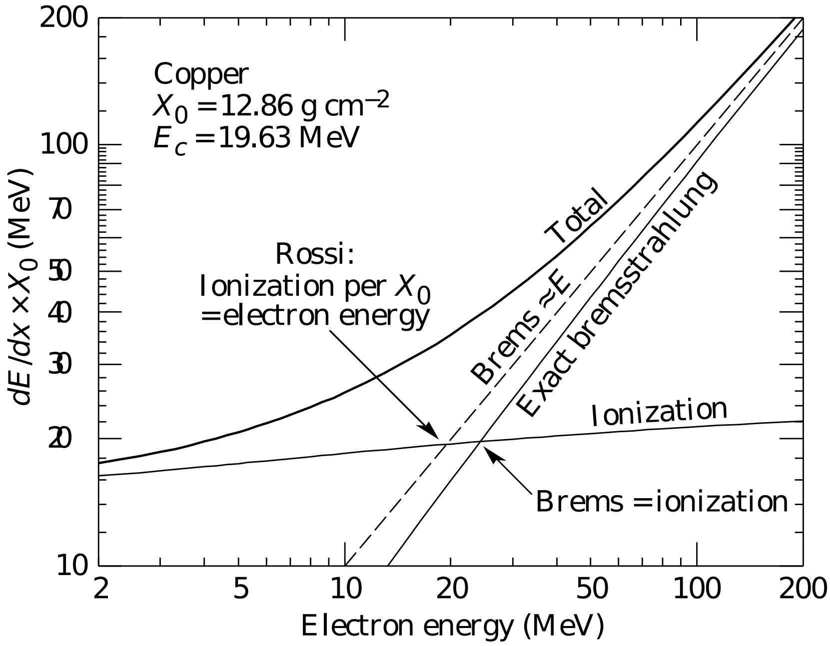

Figure 3.2. Bremsstrahlung and Ionization contributions to $dE/dx{\times}X_0$ [4].

3.2.3. Energy Loss Distribution

Bethe formula gives dE/dx averaged but the distribution of the deposited energy with a single collision is not Gaussian. For thick absorbers where the primary collision number is high, the lost energy distribution approaches to a Gaussian distribution. This can be explained with the central limit theorem, since we can assume that the underlying probability distribution for deposited energy is the same for all collisions when the change in the speed of the incident particle is very small [15].

A typical distribution can be seen in Figure 3.4. For thin layer absorbers where the number of collisions is low, the distribution is not symmetrical and has an exponentially decreasing high energy tail. Mean energy is higher than the most probable energy.

This distribution can be explained with Landau or Vavilov theory depending on the ratio of mean energy loss and the maximum allowed energy transfer $\kappa = \bar{\Delta}/W_{max}$.

Landau theory makes three assumptions; W_{max} is infinite, energy transfers are large enough that atomic electrons can be treated as free, and the decrease in particle velocity is small. These conditions are applicable if κ is close to zero (very thin absorber case).

Vavilov's theory generalizes the Landau theory for the cases where κ is not small, since W_{max} value in Vavilov's theory is finite. For very small κ, the resulting distribution approaches the Landau distribution and for the limit where $\kappa \to \infty$, it approaches the Gaussian distribution. Related formulas can be found at Seltzer and Berger [16] or in Vavilov's original paper [17].

3.2.4. Transition Radiation

Transition radiation (TR) occurs when a charged particle passes through the boundary of two materials with different dielectric constants. An intuitive example of this would be free space and conductor boundary (Figure 3.3). For this case, the actual charge and its image would act like a dipole until the particle enters into the conductor at which point we would expect some radiation.

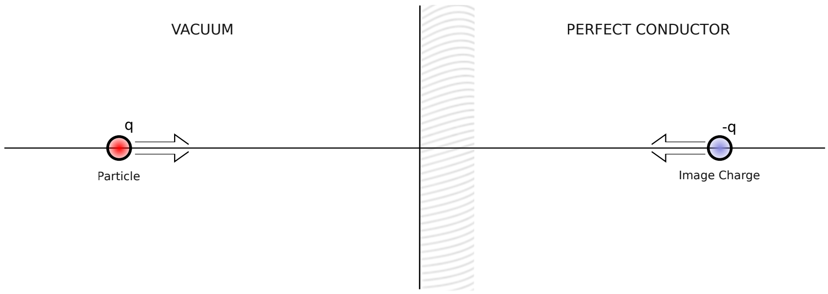

Figure 3.3. The mechanism of the transition radiation is like the behaviour of an electric dipole (for non relativistic particles) created by a charge moving towards a conductor, and its image.

At low speeds, TR can produce visible spectrum photons and this would have little use. For highly relativistic particles, TR photons can have energies in the soft X-ray regime. The emitted energy is proportional to the Lorentz factor(γ) of the particle. This proportionality comes from change in the TR spectrum rather than the change in the total photon emission probability. As γ increases, the spectrum hardens. The direction of the resulting photon is very close to the charged particle's path.

To amplify the probability of emittance photons, radiator material should have transition surfaces along the path of the particle. Many layered thin foils, fibers, foams can be utilized in order to produce more photons in this way. The γ dependence of the spectrum can be utilized in particle detectors, as means for particle identification [18].

3.3. Photon-Matter Interactions

Photons interact with matter through photoelectric effect, Compton scattering and pair production. For the region of photon energies we are interested in the scope of this study (soft x-rays), the effects of the Compton scattering are marginal and particle production needs more energy than one electron and one positron rest mass energy summed. In Figure 3.5, the contributions of these effects are presented. It is easily seen that the photoelectric effect dominates for low photon energies.

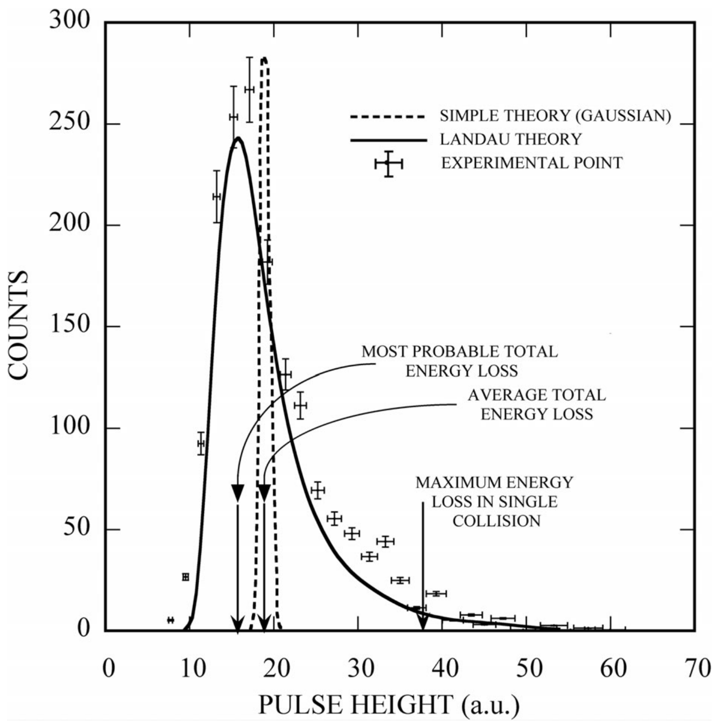

Figure 3.4. Experimental data, Landau function and the expected Gaussian distribution comparison for particles loosing energy in a thin-layer of material [5].

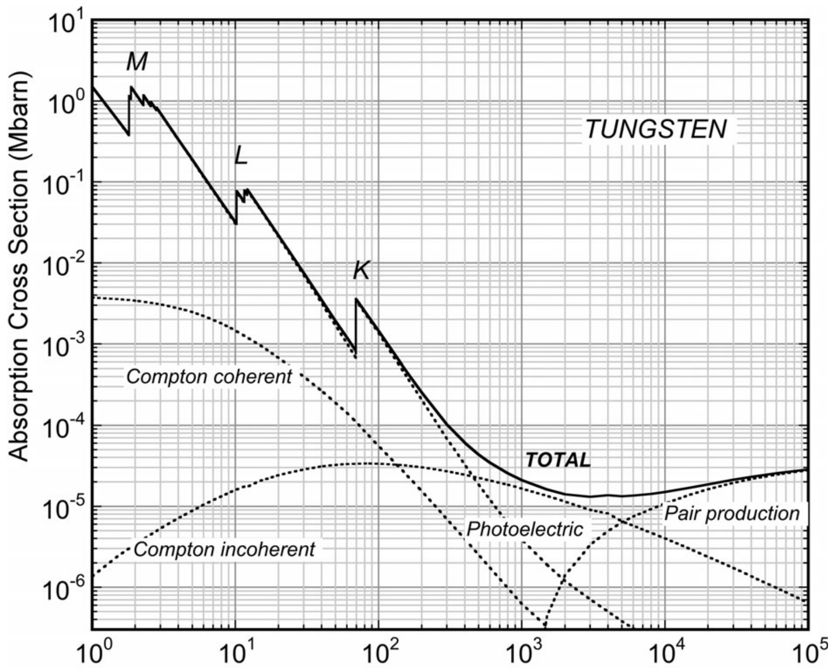

Figure 3.5. Photoabsorption cross-section for Tungsten [5]

An incoming photon which has energy greater than the binding energy of an atomic electron can be absorbed and results in the ejection of the electron with the kinetic energy :

$$E = h\nu - \text{Binding Energy}. \tag{3.5}$$

In Figure 3.5, the edges marked with the letters K, L, M correspond to the electronic shells of the atom. These sudden rises correspond to the ionization energy of the different shells.

If a photon is absorbed, and an inner shell electron is involved, the atom reorganizes itself and can emit the absorbed energy through different means like photo emission or Auger electrons, which can further interact with matter.

3.4. Creation of Ion-Electron Pairs and Effects of Electron Capture in Gas

As discussed before ionization can occur if the incident particle transfers at least the amount of binding energy of an electron of the medium. When ionization is the result of direct interaction of the particle, it is called *primary* ionization. The resulting particles may be energetic enough to cause so-called *secondary* ionizations. Even secondary ionizations can cause further ionizations if they are energetic enough.

Another ionization mechanism is the Penning Effect. Some excitations can have large deexcitation times and the excited molecule can collide with another gas molecule and ionize it. Furthermore, the formation of noble gas molecular ions can be counted as an important process.

Mean number of electron-ion pairs created depends loosely on the incident particle type. This value can be calculated by dividing deposited energy to mean-energy for ion-electron pair creation. Mean-energy for ion-electron pair creation is not equal to ionization energy since only some portion of the energy is spend for ionization.

If there is no electric field applied, the ion-electron pair attract each other and they can recombine. This process results in a photon. If the detector is based on the efficient collection of ion and electrons, the recombination becomes important. Fast recombination reduces the collected ions and electrons which will effect the efficiency and the resolution of the detector.

Another electron attachment effect occurs if the electron is captured by an electron negative atom like Oxygen. This attachment can reduce ion-electron collection efficiency drastically.

3.5. Drift and Diffusion of the Charges in Gas

Created ion-electron pairs must travel in the gas in order to be collected. To understand their movement, diffusion and drift (in an electric field) phenomena should be understood.

After a number of collisions, the created ions and electrons lose their energy and achieve thermal equilibrium. At room temperature mean speed of the electrons are of the order of 10^6cm/s while the ion speed is on the order of 10^4cm/s [15].

If there is an electric field applied, the electrons and ions will separate and start to drift apart. Electrons move towards the anode and ions move towards the cathode. On their way to the electrodes, ions and electrons collide with gas molecules and distance between two consecutive collisions determines the average drift velocity. The drift speed is slower for ions since they are much heavier than electrons. The drift speed and the diffusion are especially important in the detectors such as drift tubes where drift time (the time passed between ionization and collection) is the basis of the positional measurement.

3.6. Avalanche Multiplication and Proportional Counter

Multiplication occurs when the free electrons in the gas gain enough energy while drifting to cause another ionization. Since these newly freed electrons can produce more electron-ion pairs, multiplication of the original charge occurs. The final number of electrons divided by the number of primary electrons is called the multiplication factor. One important thing about multiplication is the electric field. If the field is not strong enough multiplication does not happen. This means by designing appropriate electrodes the multiplication region can be localized.

A cylindrical proportional counter consists of a conducting cylindrical cathode and a thin anode wire at the center. When voltage is applied across the electrodes resulting electric field gets very strong in the vicinity of the wire so the multiplication only occurs in a limited volume. Any electron that has drifted from outside of this small region will experience the same multiplication. Hence if the the multiplication region is small compared to the full detector region, the total electron ion pairs that are produced in the detector will be proportional to the amount of energy lost by the particle in gas.

A cylindrical proportional counter collects electrons very quickly, partly because electrons are light and partly because most of them are produced near the anode. The proportional counter is also referred to as the drift tube if its primary goal is to measure the drift time. In the design of the proportional chambers gas choice plays an important role. Most of the design considerations such as ionization efficiency, gas multiplication (gain), drift time and photon capture efficiency etc, change with the gas composition.

4. TRANSITION RADIATION TRACKER

The ATLAS Transition Radiation Tracker (TRT) is a subdetector of the ATLAS inner detector. It is located between the solenoidal magnet and the semiconductor tracker (SCT), and and consists mainly of small-diameter drift tubes called straws. The 122,880 straws that make up the endcaps of the TRT are 37cm in length and are placed radially. The 52,445 barrel straws are placed parallel to the beam axis, organized into about 30 layers. Altogether the TRT covers a pseudorapidity range of $|\eta|$<2 and provides 30 hits per track in this range (Figure 4.1).

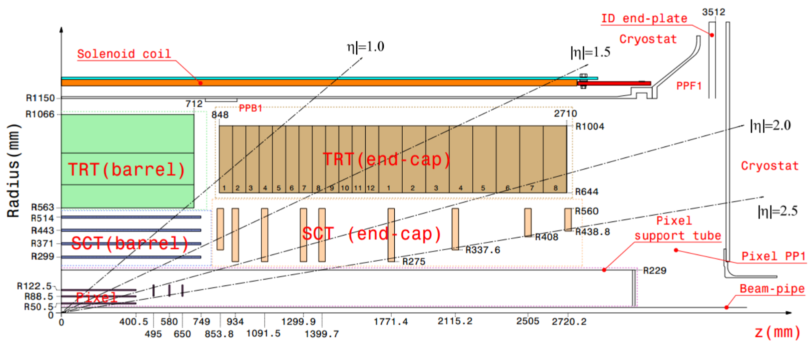

Figure 4.1. Inner detector elements [2].

The signals coming from the straws are digitized by comparing them with a low-level threshold (LT) and a high-level threshold (HT). A schema of the signal and digitization is shown in Figure 4.2.

The LT bits are used in drift time and time-over threshold calculations, whereas the HT bits indicate TR-photon capture and are used in particle identification (PID).

4.1. Straws

TRT straws are made with reinforced tubes of 4 mm diameter and a gold plated tungsten anode wire of 30 μm diameter. Tube walls are roughly 80 μm thick and made of coated Kapton (Figure 4.3.b). The coating of the Kapton film is aluminum with

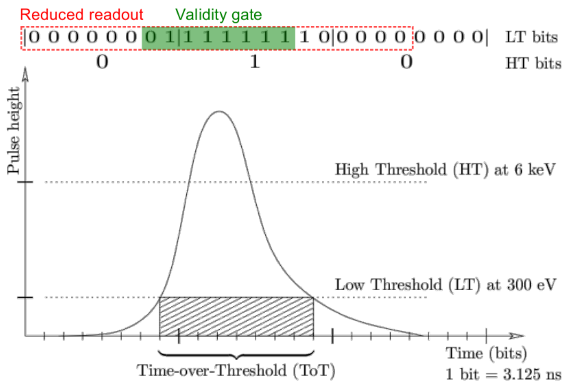

Figure 4.2. TRT signal and its digitization [6].

a carbon-polyimide layer on the one side, and polyurethane on the other side. The film has been cut into 10mm wide tapes and wrapped using a mandrel as shown in Figure 4.3.a. The heat which is applied with mandrel, activates the adhesive property of polyurethane and two tapes bond together. The aluminum coating makes the walls electrically conductive. Carbon−polyimide functions as a protection against discharges and cathode etching. Lastly, straws are mechanically reinforced with carbon-fibre bundles. The completed straws have good mechanical properties, they support the radiator material in the barrel and the internal structure in the endcap wheels. [7]

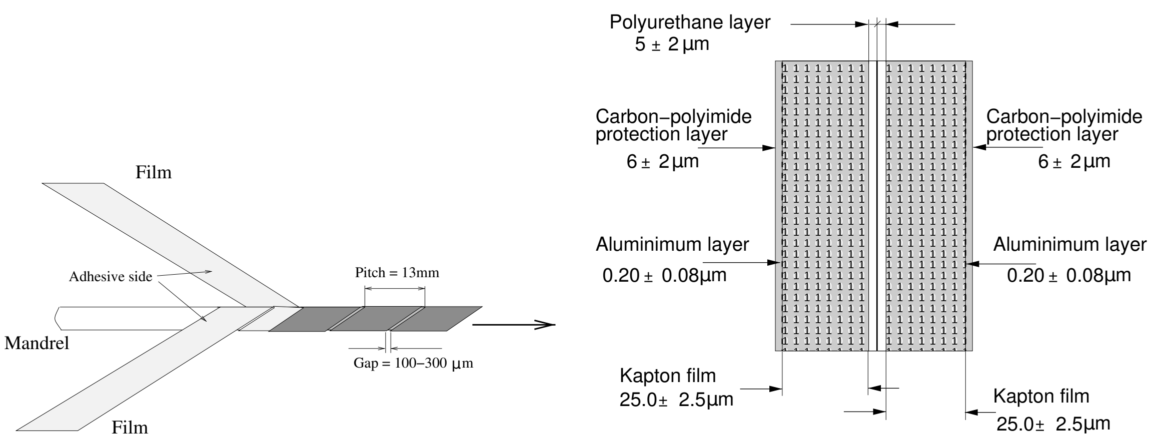

(a) Straw Production Schema

(b) Straw Wall Section

Figure 4.3. TRT Production and Straw Wall Design. [7]

While the endcap straws are read from one end, the barrel straws are read from both ends. The anode wire of each barrel straw is split into two or three sections which are electrically isolated from each other. For the straws in the innermost 9 layers the anode wires are split into three, with the center region of length 80 cm not connected to the outside, i.e. there is a dead zone. This is meant to keep the occupancy of those straws at an acceptable level. The straws from the outer barrel layers have their anode wires split into two at the center and each subsection is read out separately from the two ends.

TRT straws walls are kept at about -1.5kV while the anode wires are kept at 0V, resulting in a gas gain of $\sim$2500.

4.2. Gas Mixture

TRT straws were initially meant to be filled with a Xe based gas mixture to capture TR photons efficiently. The mixture in LHC Run 1 was a Xenon, CO_2 and O_2 mixture ($Xe/CO_2/O_2$: 70/27/3). During the LHC Run1, some cracks emerged on the TRT gas pipes and some of this damage was irreparable. Because of the unavoidable leaks, gas composition used in the affected parts was replaced with a relatively inexpensive Argon-based composition.

Since the TR photon capture performance of the Argon gas is limited, Argon filled straws have lower HT probability therefore the PID aspect of the TRT affected. It is worth noting that despite the gas leaks, tracking performance was not affected. [6]

4.3. TRT DAQ-Electronics

The straws produce a signal amplified with avalanche multiplication. In order to read this signal two chips on the front-end, which are called Amplifier/Shaper/Discriminator with Baseline Restoration Chip (ASDBLR) and Drift Time Measurement Readout Chip (DTMROC), work together.

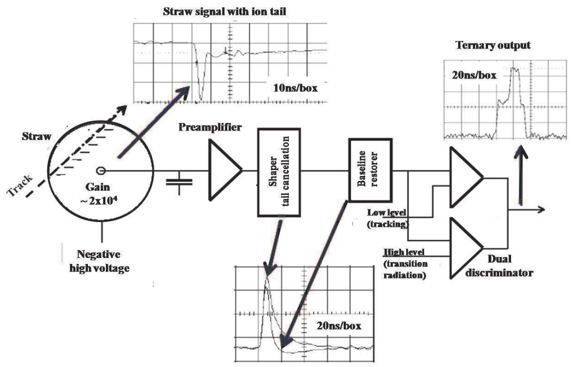

Figure 4.4. Signal processing with DTMROC chip [8].

ASDBLR chip takes drift tube signals, amplifies and inverts them, discards the signal tails, restores the base line, and then compares the signal against the two thresholds. Output signal is a three-level differential current signal as shown in Figure 4.4. DTMROC takes the output of the ASDBLR and digitizes it. Also it controls some aspects of the ASDBLR chips like the threshold values and generates test pulses. The digitized data from DTMROCS is delivered to the TRT readout drivers via patch panels. Each ASDBLR chip can be connected up to 8 straws and each DTMROC can be connected to two ASDBLRs. [8]

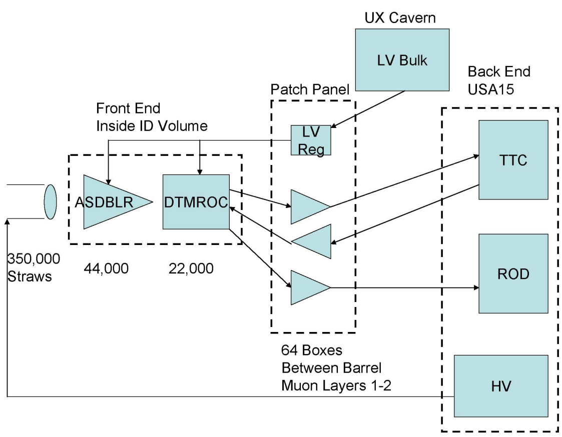

Figure 4.5. Overview of the TRT electronics [8].

4.4. PID and HL Probability

As discussed in the previous chapter, TR spectrum hardens with increasing speed of the particle (γ), usually leads to a rise in detectable TR photons creation probability. An electron, since it is much lighter than a pion, will have higher γ factor when compared to a pion of the same momentum. In a certain energy range, these two facts can be used to help particle identification (PID).

TRT high level (HL) hit probability increases if the detectable TR emission probability rises, yet it is also depedent on many other factors like TR photon capture probability and high energy deposition by the charged particle, etc. Therefore it is effected by various parameters like the type of gas used. Regardless, as the γ versus high threshold probability plot in Figure 4.6 shows, this probability can help to distinguish between pions and electrons in the momentum range of 1 to 200 GeV. When the momentum is lower than 1 GeV, electron HT probability is too low and higher than the 200 GeV, pions also start to produce significant HT hits.

The high-level to low-level hit fraction (HL hit fraction) can be used in particle identification (Figure 4.7). In LHC Run1 transition radiation measurement was amongst the parameters used in tight electron selection criteria. It has also been used in various studies like the measurement of W boson production cross section [9].

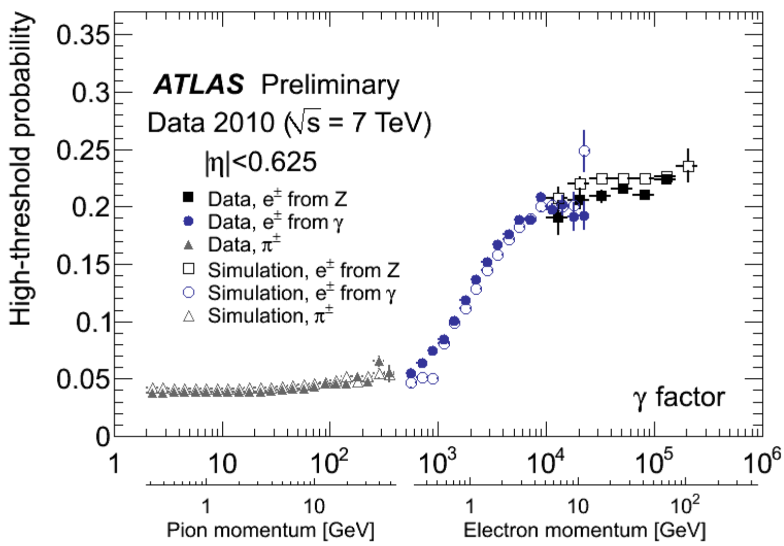

Figure 4.6. High Threshold probability versus the Lorentz factor in the barrel region of the TRT [9].

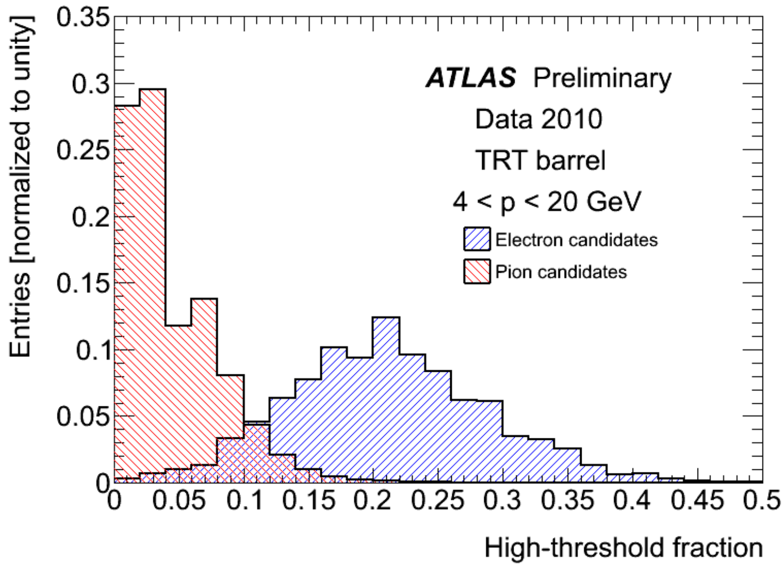

Figure 4.7. HL hit fraction for electron and pion candidates in the barrel region of the TRT [9].

5. 2015 TRT TEST BEAM

5.1. Test Beam setup

In this chapter we describe the test beam run that was held at CERN (SPS north area H8) during 26^{th} May-1^{st} June 2015. The main goal of this effort was to understand TR photon capture performance with Krypton gas mixture. Since with the real TRT detector we have limited time for test during the physics runs, choosing parameters (high-level threshold value) needed data from such a specific effort. The effort also aimed to test different gas mixture - radiator - pressure combinations. As a result this work aimed to improve our understanding of the effects of various factors on TR performance.

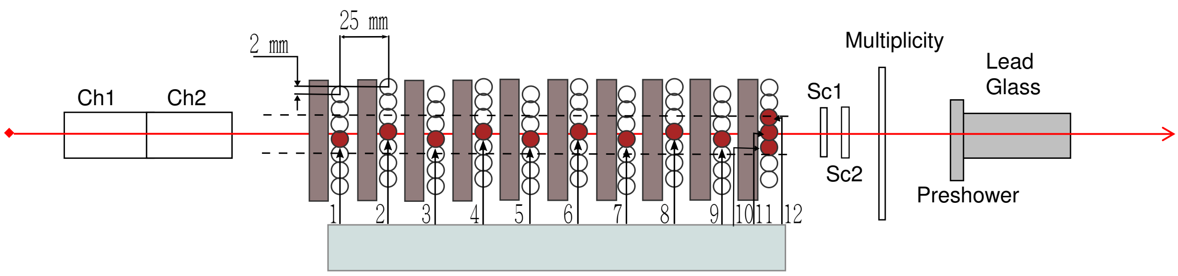

Figure 5.1. 2015 TRT Test Beam Setup

The planned test beam setup consisted of two $1cm \times 2cm$ scintillators (Sc1 and Sc2 in Figure 5.1), a multiplicity detector, a 17-radiation-length lead glass calorimeter with a 5mm thick lead target in front for preshower and two Cherenkov detectors (Ch1 and Ch2) filled with He gas. The TR part of the experiment is a dedicated setup which is made out of TRT straws. Except being shorter (15 cm) they are the same as the ones in TRT and 12 of those (marked in the figure with red circles) were used for data taking.

5.2. Timing and Cables

Due to some noise whose origin could not be identified during the test beam runs, the discriminators that were connected to the TDC had to be set to higher thresholds than usual, which allowed the TRT experts to declare the straw conditions as nominal. However this meant that time measurements coming from straws were corrupt. Hence we have not included time information in the analysis. (If we had used the TDC measurements, we would have introduced some intrinsic and complicated energy cuts.)

5.3. Triggers

The setup had mainly two types of triggers: one is the calibration trigger which would trigger the data taking if any of the 12 straws registered a signal above a threshold. With the calibration trigger, both the pedestal and ^{55}Fe radiation data were acquired at the same time. For the data taking part with the beam, coincidence of signals from the two scintillators were used to define the trigger. The cross-sectional area of the scintillators was roughly the size of the beam. Appropriate photo multiplier tubes were facilitated to measure the scintillation. The trigger efficiency was 100%.

5.4. Online monitoring for the test beam

To be able to respond to any changes from the nominal conditions of detectors installed, the testbeam monitoring was used. The software for this task was written ground up with c++ using existing ATLAS monitoring and BL4S (Beamline for schools: a competition for high-school students) frameworks. The graphical user interface (GUI) of this code can be seen in Figure 5.3. The GUI was based on the ATLAS software framework's online histogram presenter (OHP). In order to present relevant histograms a configuration file was written. Main goal was to sample the events as much as possible and get the idea of the current status of the detectors. This was crucial since beam time is valuable and detecting problems after run would cost significant loss of time. Monitoring had raw outputs of all the TDC and QDC channels as histograms as well as simple calibration to see the rough dE/dx measurements of the particles through the straws and the TR effect. It can be considered essentially as a crude prototype of our analysis. Because of the low rates of events and highly efficient data acquisition, all the events could be sampled online.

The code was written in a modular way that allowed it to be used later for offline monitoring as well. It was about 1000 line long. The selection and calibration values were extracted from a text file. In this way, any change on the parameters could be applied readily.

5.5. Offline monitoring for the test beam

A bash script was implemented that ran a crude analysis and produced report files in PDF format (Portable Document Format). This script was made accessible through a graphical user interface that allowed the shifters to run it after each run by clicking a desktop icon. If the run was for calibration the shifter would printout calibration, plots which are mainly straw spectra zoomed around pedestal QDC range and ^{55}Fe QDC range. An example can be seen in Figure 5.2. For data taking, the

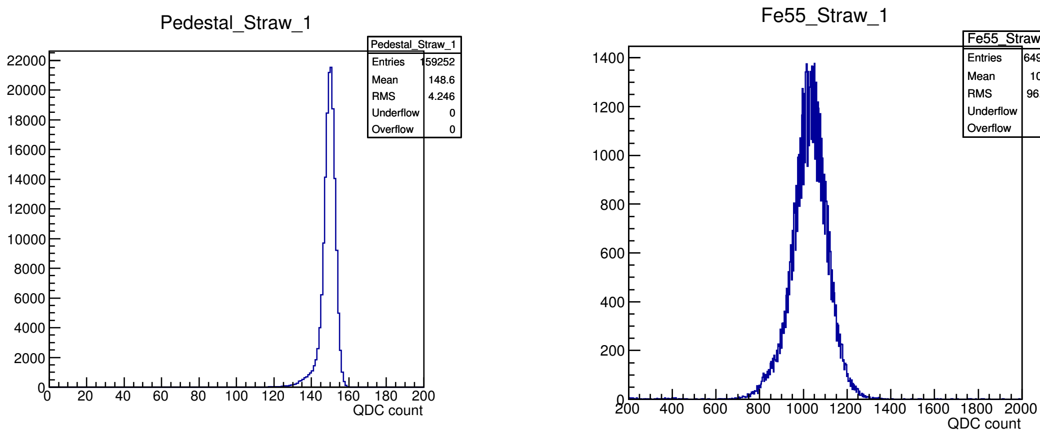

(a) Pedestal zoomed

(b) ^{55}Fe zoomed

Figure 5.2. Pedestal and ^{55}Fe spectrum zoomed [10]

shifter would examine the plots needed for data analysis. Printed reports were used in discussions all along the test beam and afterwards.

Figure 5.3. An example screenshot from the online Histogram Presenter used in Online Monitoring [11].

5.6. Gas gain

Gas gain of the straws is tied to lots of outside parameters, such as temperature, the pressure (input and output), gas mixture and so on. We did not have control over temperature and had limited control of some of the environmental parameters. As a result, the effective gas gain would drift if the high voltage was to be kept constant. To monitor any changes, a fast oscilloscope calculated the signal amplitude of a dedicated straw which was constantly radiated by a radioactive source. Shifters would regularly control the gas gain and by manipulating the high voltage supplied to the straws, they would keep the gas gain constant within a certain range as demonstrated in Figure 5.4.

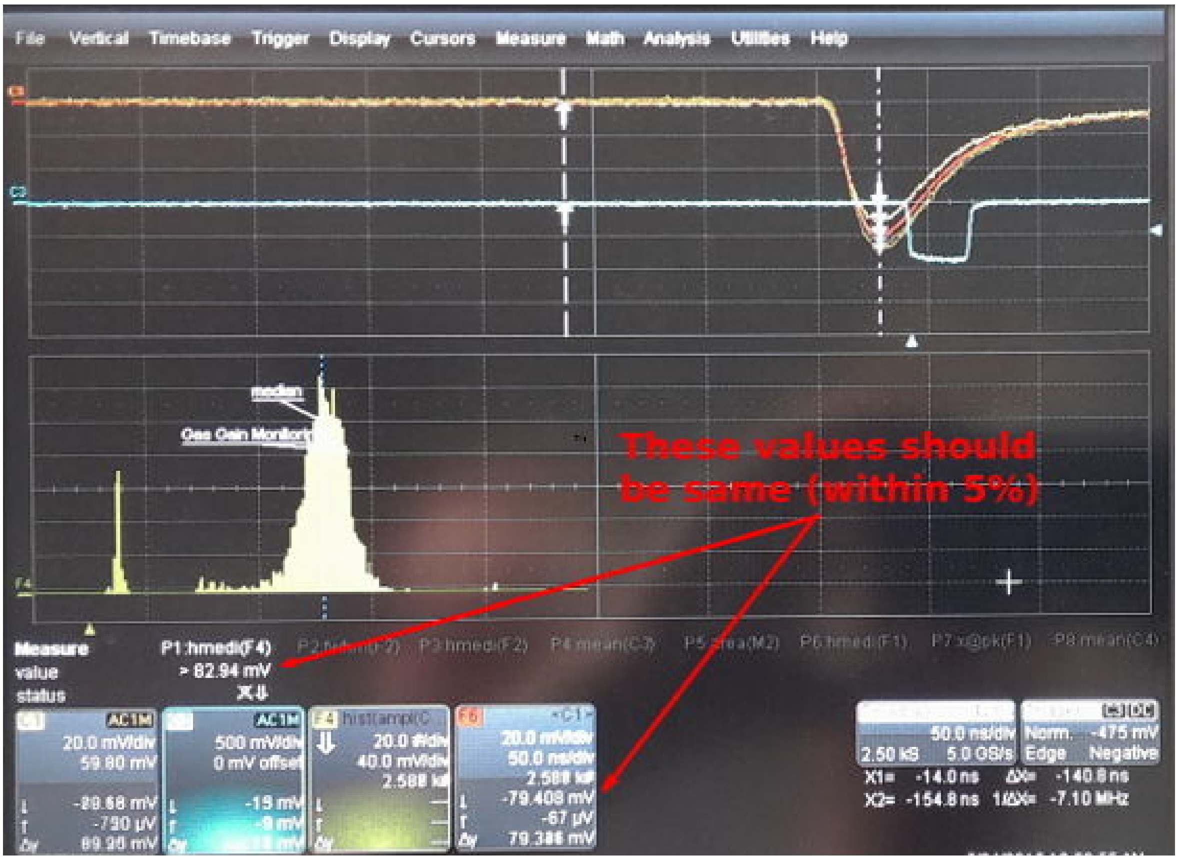

Figure 5.4. Example oscilloscope screenshot, as it was being used for gas gain monitoring [11].

5.7. Gas mixtures and beams

We had three different gas mixtures with Xe, Ar and Kr as the noble gas. Xenon is the main choice as the operating gas because of its good TR photon capture. Argon was expected to have lower TR photon capture efficiency. Krypton was in between of those two, as can be inferred to by looking at the absorption lengths (Figure 5.5) of the gas for the spectrum of photons we get as TR(4 keV - 30 keV).

Based on chromotography measurements, the composition of the Xe gas mixture was $Xe/CO_2/O_2 = 71.8\%/25.6\%/2.6\%$ and the other mixtures were close to this.

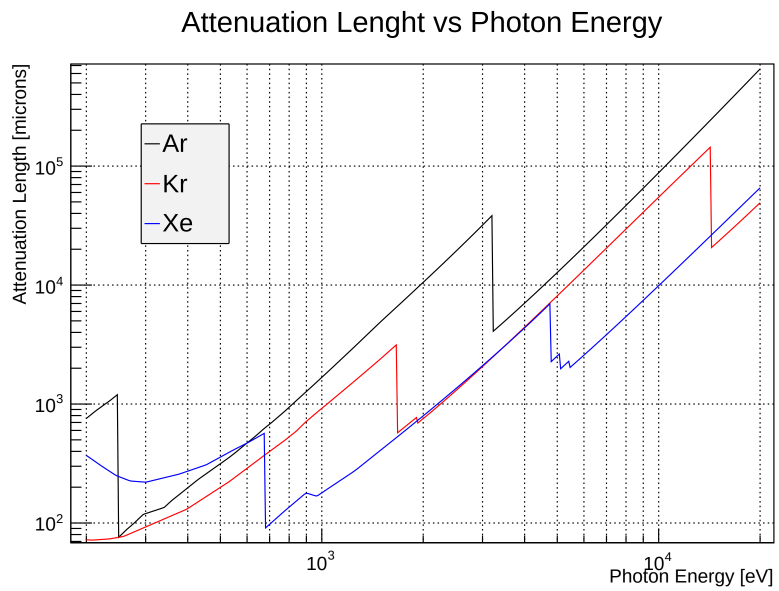

Figure 5.5. Attenuation Length vs Photon Energy graph for Xenon, Argon and Krypton gas at NTP. Data from [12]

SPS delivered two types of beams. One was electron-rich and the other one was pion-rich. The electron-rich beams were a result of a lead target bombarded with a proton beam and selecting 20 GeV. For the pion-rich beams, a copper target was used. Unfortunately the actual detailed compositions of the beams were unavailable. Moreover, the rate was lower than what was expected and because of that we had take longer runs and still collected reduced statistics.

5.8. Radiators

- Polypropylene film (8 mm thick),
- Fibre radiator (8-mm thick foam),
- No radiator configuration

During the tests we had different types of radiators and with different layouts but for the subject of this thesis, we will only focus on the cases where a layer of radiator (either foil or fibre) was placed in front of each group of straws (as seen in Figure 5.1), since those setups resemble TRT most.

6. ANALYSIS

6.1. Particle Identification and Selection Criteria

To study differences between the pion and electron responses of the TR detector, we must first identify these two. In the 2015 test beam, the runs were a mix of electrons and pions; most of which were electron-rich and a few rich in pion. Since the Cherenkov detectors of the test beam setup were not working properly and reliably, we had to use our own detectors to identify the particles.

In this study having some pion-rich runs was really helpful to observe the differences and decide on the selection criteria. Since pions interact modestly with both lead-glass and the preshower calorimeters we would expect their effect as low QDC counts whereas electrons would produce high QDC counts. This effect can be seen, when electron-rich and pion-rich runs are compared in Figures 6.2.a and 6.2.b. In the electron-rich runs one can observe a broad distribution on preshower and a peak around 2200 QDC count in the lead-glass calorimeter. These two distributions clearly demonstrate the characteristics for electrons, as the pion-rich runs mostly lack similar features.

The lack of different-composition runs beyond the two types mentioned above overrules the possibility of a quantitative study of the beam composition in an attempt to determine the amount of possible contamination from other particles, such as protons and kaons. If these contaminations were of a significant level, we would expect to see the tail of a decaying function underneath the sharp electron peaks in the lead-glass calorimeter QDC count histograms. As no such strong feature is observed we qualitatively conclude that contaminations appear to be negligible for the electron-rich runs and manageably-low for the pion-rich runs.

In order to reduce whatever small contaminations exist, and to separate electrons from pions, we introduce selection criteria in the preshower-lead-glass QDC-count plane as shown in Figure 6.3. The electron cut is shown with the blue rectangle, whereas the pion cut is in red.

As an additional crosscheck of the amount of the contamination, the region between the peaks in lead-glass histograms seen in Figure 6.2 are compared. The two histograms were normalized to have the same size pion peaks (first peak), and then the region to the right of that peak was studied. While we observed some discrepancy, it was quite small and the compositions were concluded to be mainly pions and electrons. Finally, it is worth mentioning that more strict cuts were tried later on as an exercise, but the difference in the final results were small and within the statistical uncertainties.

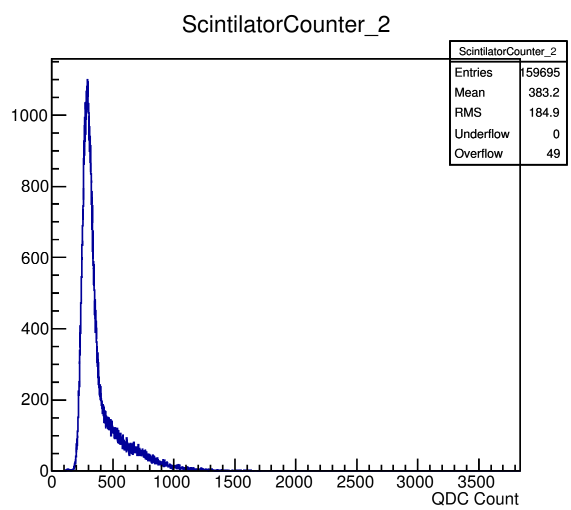

Figure 6.1. Scintillation Counter 2 QDC value histogram

For clean up purposes a selection criterion is applied on the Scintillation Counter (Sc2) QDC values (Figure 6.1). Events that have Sc2 QDC counts between 200 and 400 are selected for analysis. Particles with the lead glass QDC values between 0-1500 and preshower QDC values between 200-300 are taken as pions. Particles with the lead glass QDC values between 2000-2500 and preshower QDC values between 400-3500 are taken as electrons. Furthermore straw hits with energy value smaller than 0.055 keV are rejected throughout the study. The purpose of this small cut is to get rid of remaining pedestal values after calibration from the results.

Before describing the calibration and analysis procedures, it is wort mentioning that for the rest of this thesis, only the data from Straw 11 were used in the study of the electron energy deposition spectre, but the data from 9 out of 12 straws were used in the study of pions. (Straw 6 was not working properly. Straws 10 and 11 were not being illuminated fully.)

The reasons for this choice are as follows:

(i) Straw 11 is the furthest away from the point of entry of the beam into the TRD, with TR build-up from many layers of the radiators having reached a saturation value. This is similar to the situation with the actual TRT which has many concentric layers of straws.

(ii) Pion have low statistics in our test beams and hence it is useful to accumulate the data from all the straws. This procedure can be safely applied as we expect insignificant TR from pions.

6.2. Calibration of Straws

In this analysis one of the main goals is to measure the effects of different gas mixtures on TR photon detection. To this extent we start with studying the distribution of the QDC counts from the straws. These values are correlated with the energy deposition in the straws given that straws work in proportional mode with constant gas gain. To calculate the corresponding energy deposition for a given QDC value of the channel one must use calibration data. The calibration data were taken in the presence of the ^{55}Fe x-ray source. The source was located above each straw separately for about 30 seconds at a time, while the calibration trigger was active. The QDC reading for each straw was then recorded in histograms, which showed two peak: one for the pedestal value when the ^{55}Fe was aligned with other straws (Figure 5.2.a) and the other when ^{55}Fe was directly above the given (Figure 5.2.b).

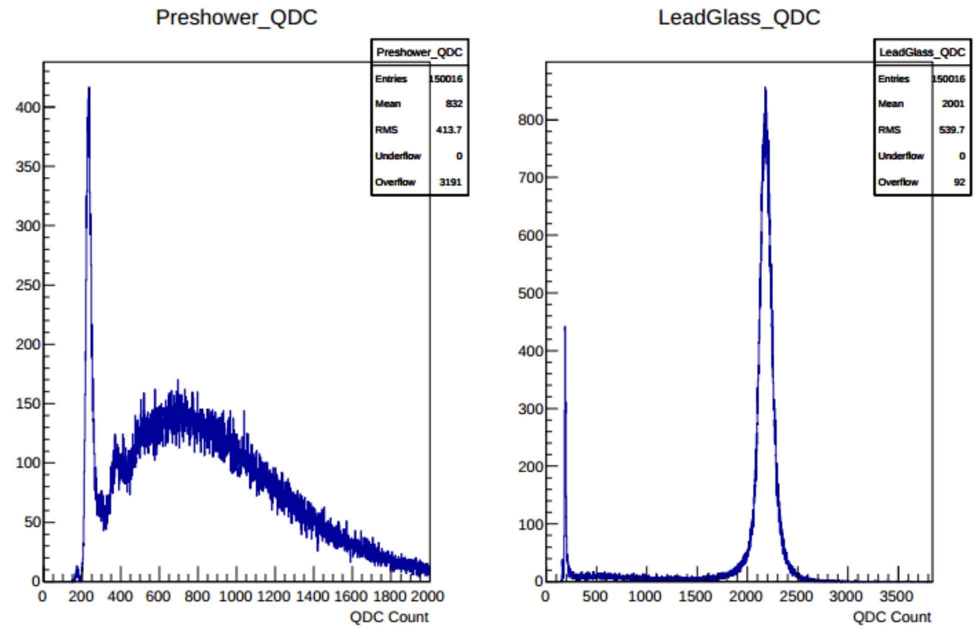

(a) Electron Rich run

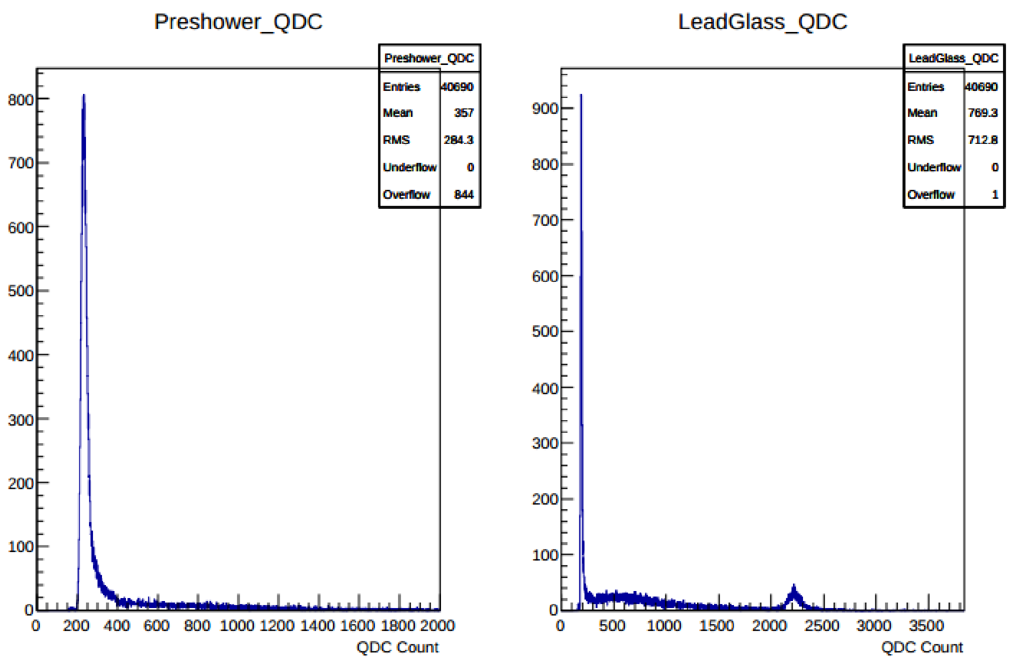

(b) Pion Rich run

Figure 6.2. Lead glass and Preshower detector QDC values for e^- rich run and π^- rich run

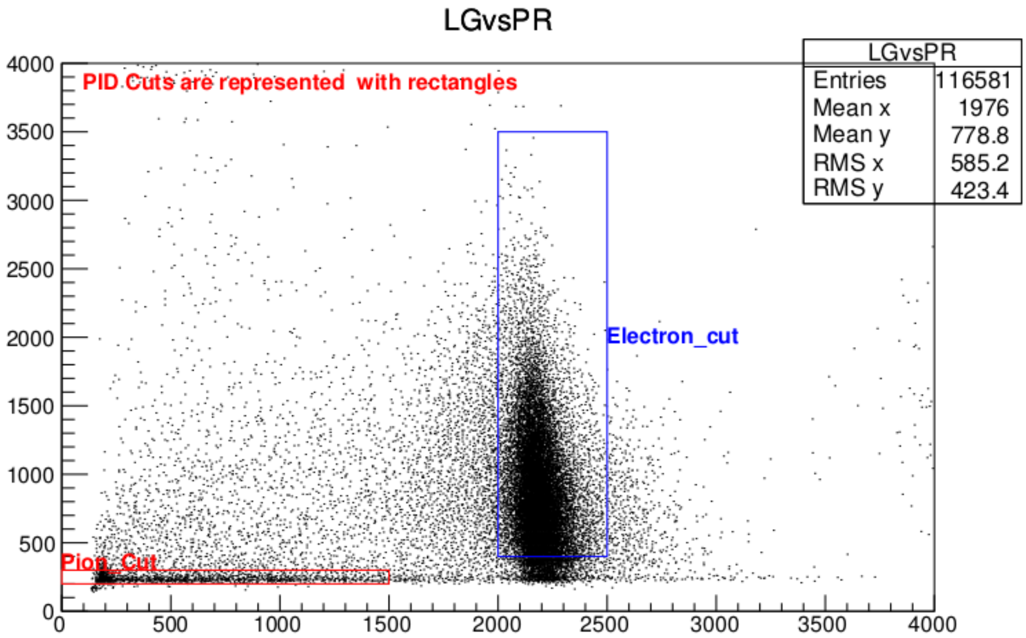

(a) Electron Rich run

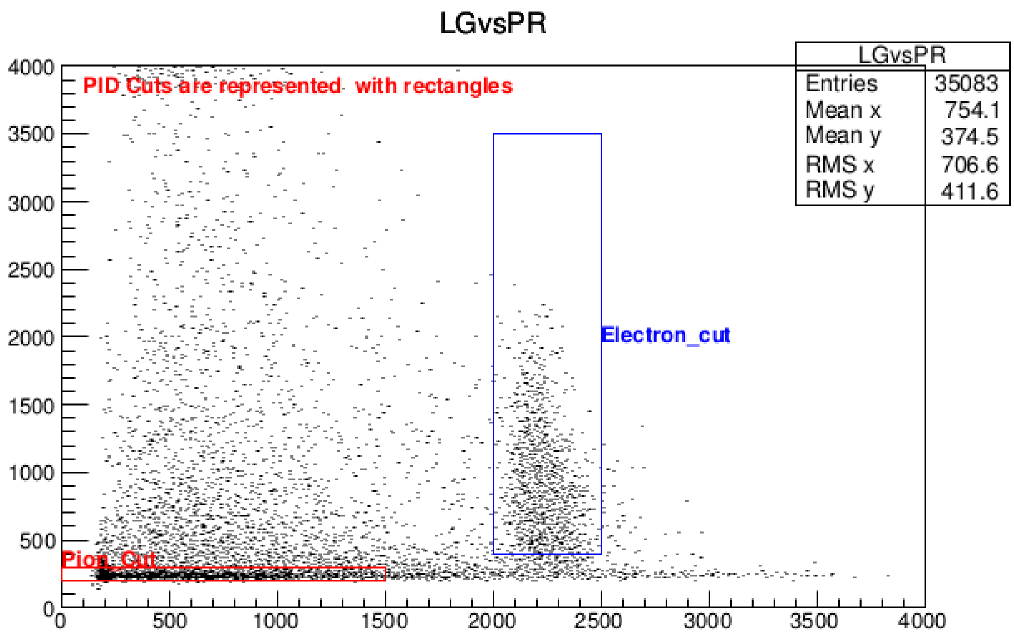

(b) Pion Rich run

Figure 6.3. Lead glass vs Preshower detector QDC values for e^- rich run and π^- rich run shown with PID cuts

Studying where these two peaks were located allowed the determination of the calibration constants separately for each straw.

The peak observed in pedestal part corresponds to zero keV deposited energy since this data correspond to no radiation on straw tubes. The ^{55}Fe peak corresponds to soft xrays from $K_{\alpha 1}, K_{\alpha 2}, K_{\beta 1}$ emissions and since these emissions are very close in energy, they manifest as one peak in the energy resolution of the straw tubes. We take this peak value as to 5.95 keV. The peak positions in the histograms were extracted from Gaussian fits.

As a result for a given QDC value the corresponding energy is determined as:

$E = 5.95keV \times (QDC - n_{pedestal})/(n_{Fe55} - n_{pedestal})$ where $n_{Fe55}(n_{pedestal})$ is the position of the ^{55}Fe (pedestal) peak.

The calibration procedure was repeated before and after each change and flushing of the gas composition. The purpose was to asses the possible drifts in the calibration. In the Xenon run, the observed change in the calibration was under 1%, while in the other runs it was higher. Upon investigating the calibrated straw energy spectra of different runs for different radiators we saw this change was different in magnitude for each data taking. To reduce the impact of this calibration issue during the analysis of the beam data, the calibration constants for a set of runs with identical gas composition were tweaked by a small amount (not more than 3% of its value) for each run, using the following procedure:

(i) We use events that pass the pion identification cut.
(ii) Those events we take the no-radiator spectra as the baseline, since the no radiator runs were taken right after the calibration runs.
(iii) We focus on the $\sim$ 2-3 keV region (as TR photons are not expected below 4keV) in the calibrated energy spectrum and compare no-radiator data with data from other configurations until they match the no-radiator data.

This procedure was applied for all runs, except for the Xe runs, as the drift in the calibration for Xe runs were observed to be less than 1% as mentioned earlier.

After the tweaked calibration, differential spectrum plots were in good shape and we could perform comparisons since we had agreement in the peak positions.

6.3. High Level Threshold Probability

Deposited energy values from straws generally contain lost energy value of the passing particle and energy deposition of the transition radiation photons produced when particle passes through the radiator. As discussed in the previous chapters energy loss mechanism of a charged particle is probabilistic and W_{max} is big enough so that we can have particles depositing energies of order ∼10keV, furthermore the TR photo emission and absorption also probabilistic in their nature. TR photons will be ejected to a direction very close to incident particle direction. As a result we observe a combination of ionization coming from a particle and TR photon, we do not have a distinct TR photon signal.

TRT compares the signal against a high-threshold value. Information of whether this threshold is achieved is indicative of a TR photon. Because of this reason the value of the high-threshold is important. To understand the TR performance of the mixtures, the probability of an electron or a pion to provide a signal above various values of the threshold needs to be studied.

In the analysis part we first looked at the Xenon based gas mixture. This gas mixture is close to what was used in LHC Run1. Calibrated QDC plots will be referred as differential spectrum through out the text since after calibration values denote deposited energy. Figure 6.4.a, shows such a plot superimposed with different radiator types for electrons. Those different radiator cases have roughly the same number of events but to judge the differences easily, they have been scaled so that their peak values coincide.

In this plot one can see a change on the deposited energy with radiators placed starting from ∼4keV. This means two things: TR photon spectrum starts around 4keV and two types of radiators produce similar TR photon spectra.

To investigate different thresholds one can produce integral spectrum which is the plot of the integral of the differential spectrum for values greater than that threshold normalized by the whole spectrum integral. In short y axis corresponds to probability to exceed threshold and x axis corresponds to different threshold values.

In the Figure 6.4.b one can see an example of a such plot: Pion no radiator case, electron no radiator case and the two electron radiator cases for the Xe mixture. This plot is a good point to start investigating the threshold values. For example the probability to exceed a 6 keV threshold for electrons without radiator is ∼0.08 (and for pion, it is ∼0.04). Upon adding radiator to the system this value changes to ∼0.23. To compare the probability-to-exceed-threshold for electrons, P_{e^-}, with that of the pions, P_{π^-}, we prepared a P_{e^-} vs P_{π^-} plot. One important remark is all P_{π^-} for a specific gas comes from no-radiator runs of that gas composition. In this way effects of possible contaminations are reduced for pions.

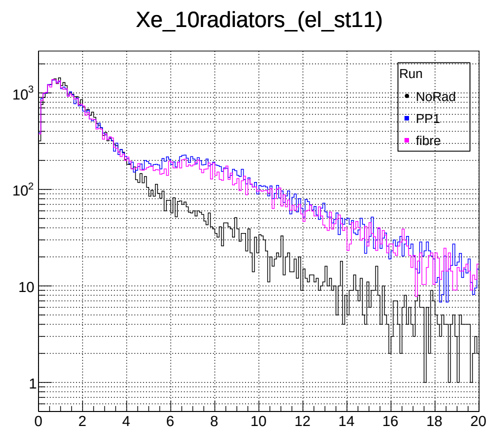

(a) Differential Spectrum

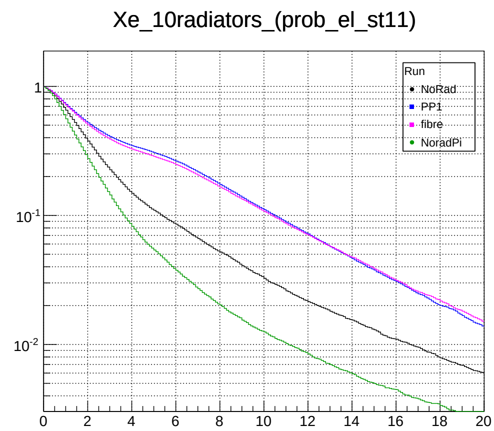

(b) Integral Spectrum

Figure 6.4. Differential and Integral Spectrum for Electrons from Straw 11 with the Xenon gas mixture. The x-axis is the Calibrated deposited energy(keV).

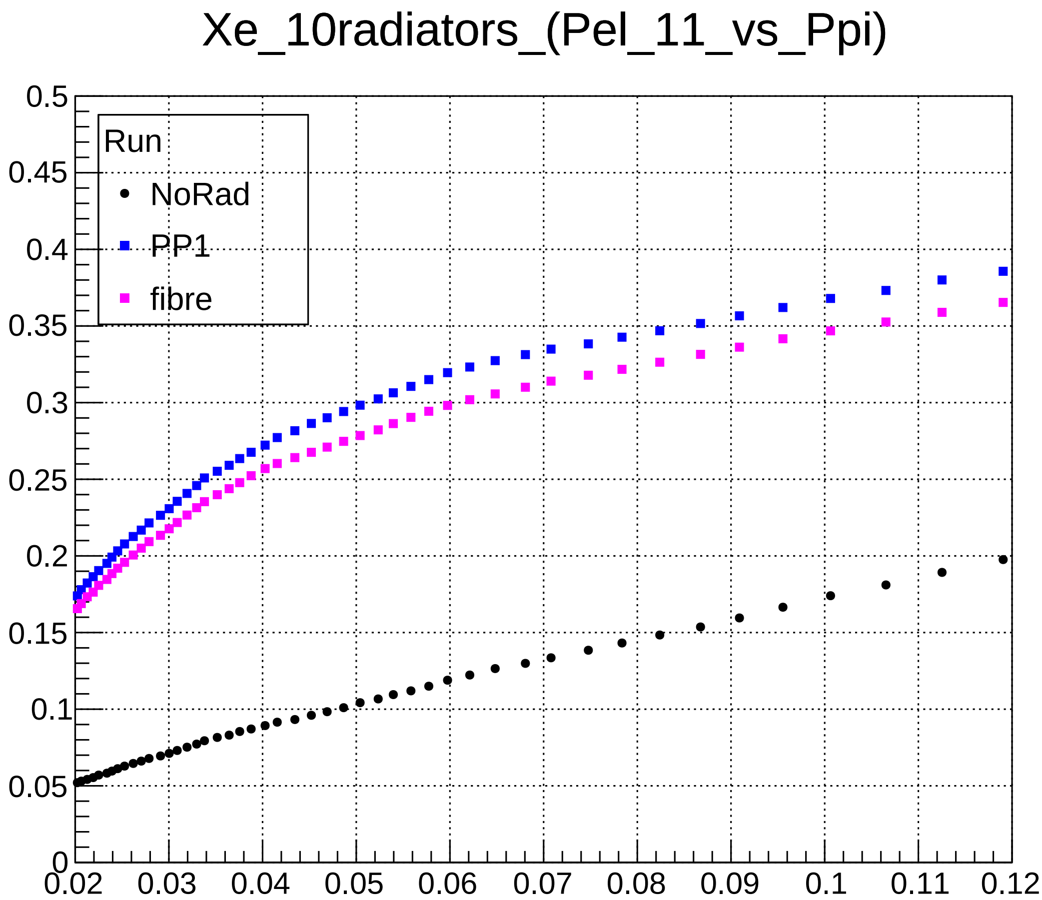

Figure 6.5. Exceeding threshold probability e^- vs π^-, Xenon.

We perform this study on Ar-based and Kr-based gas data and one can refer to appendix for the relevant plots. To compare the actual performance of the different gases we finally combine the P_{e^-} vs P_{π^-} plots for no-radiator (Figure 6.7) and for radiator-present (Figure 6.6) cases. The results favor the Kr-based mixture over the Ar-based mixture as a substitute in terms of the TR performance.

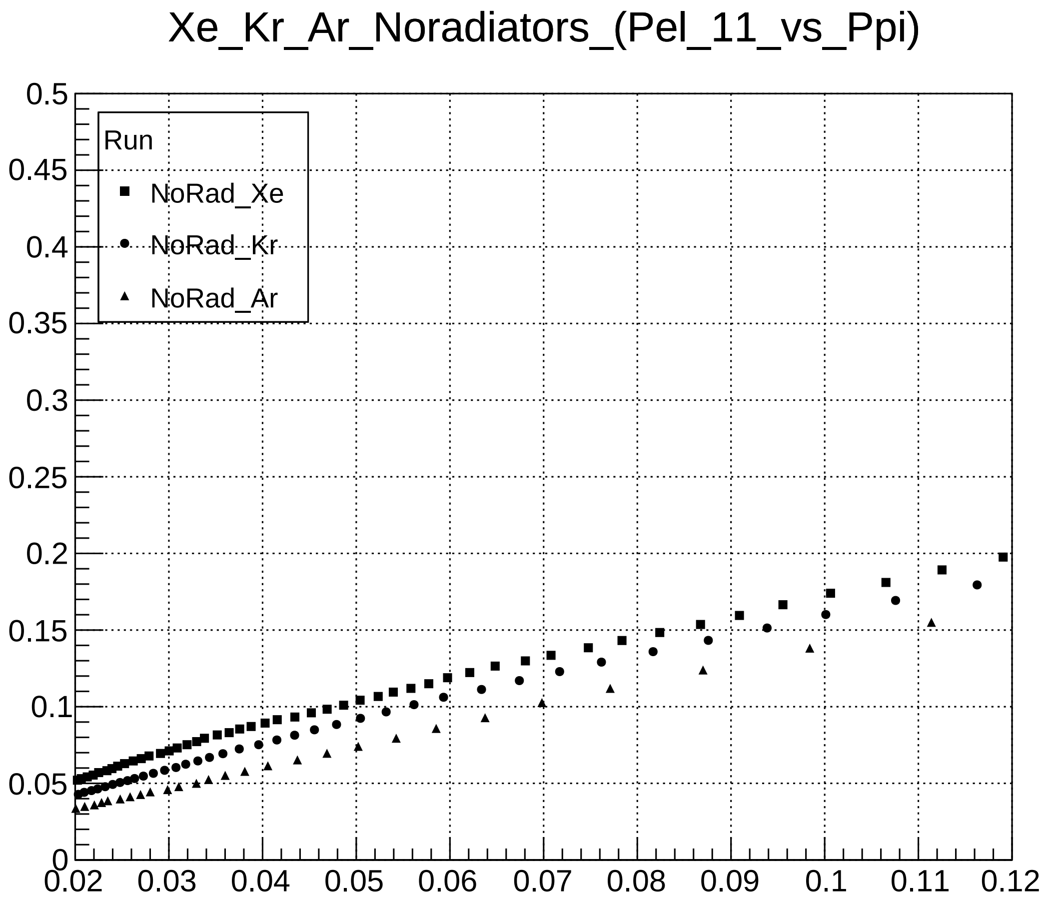

Figure 6.6. Exceeding threshold probability e^- vs π^- for Xenon, Krypton, and Argon gas mixtures (no radiators).

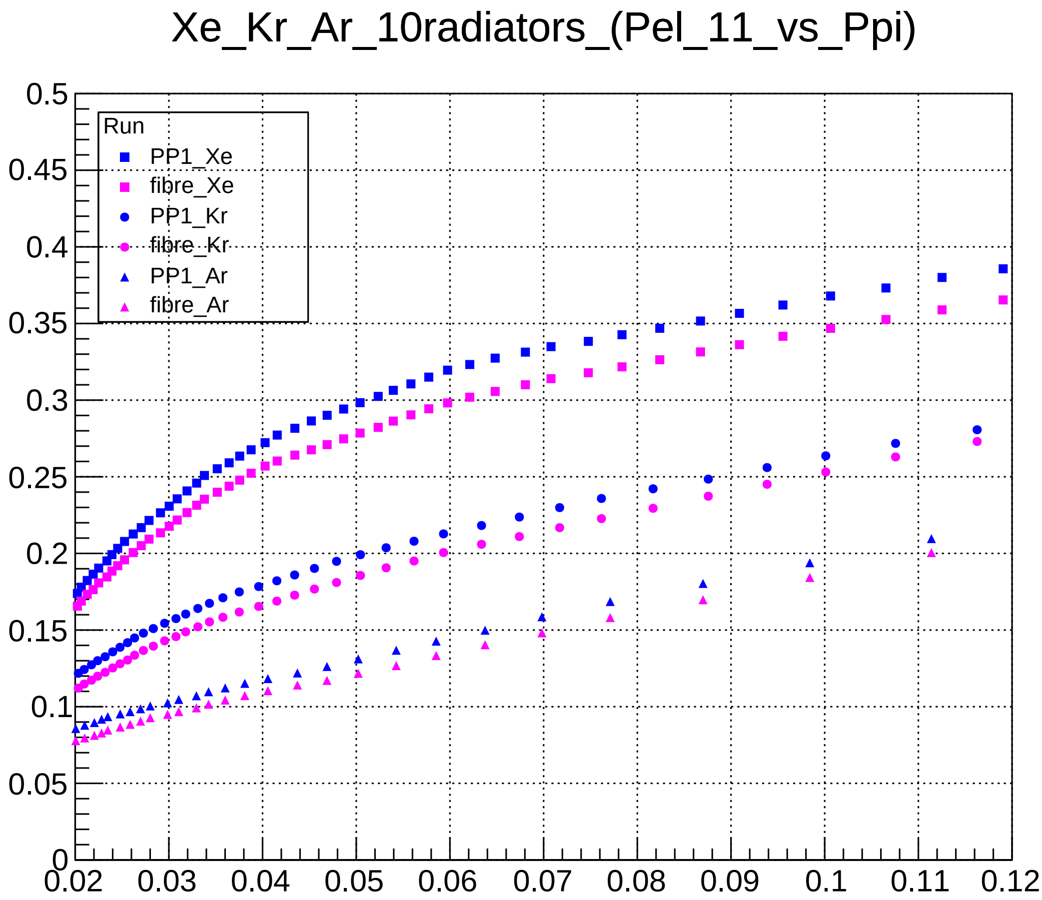

Figure 6.7. Exceeding threshold probability e^- vs π^- for Xenon, Krypton, and Argon gas mixtures (with radiators).

7. CONCLUSION

Transition radiation tracker (TRT) has been an essential part of the ATLAS tracker, providing a large number of tracking hits in addition to transition radiation measurements contributing significantly to electron-hadron identification. Recently it has become crucial to study alternatives to its default Xe gas mixture. In order to study the alternatives, namely Kr and Ar, a test beam study was performed in 2015 with a small transition radiation detector (TRD).

In this thesis, we have described this system and the work undertaken to obtain and calibrate data from it. After the calibration, an analysis was performed to obtain high-threshold TR probability plots that will allow us to determine the operating point for TRT straws with alternate gas mixtures. The actual decision for choice of such operating points require a detailed Monte Carlo simulation of the TRD, which is beyond the scope of this thesis. However, our results are in agreement with the theoretical expectations: we have observed that the Krypton gas mixture is better than the Argon gas mixture for TR photon capture, but its performance is not as good as the default Xenon mixture.

REFERENCES

1. Haffner, J., “The CERN accelerator complex.”, October 2013, http://cds.cern.ch/record/1621894, accessed at July 2016.

2. The ATLAS Collaboration, “The ATLAS Experiment at the CERN Large Hadron Collider”, *Journal of Instrumentation*, Vol. 3, No. 08, p. S08003, 2008, http://stacks.iop.org/1748-0221/3/i=08/a=S08003, accessed at July 2016.

3. ATLAS Collaboration and others, *2015 start-up trigger menu and initial performance assessment of the ATLAS trigger using Run-2 data*, Tech. rep., ATL-DAQ-PUB-2016-001, CERN, 2016, url: http://cds. cern. ch/record/2136007, accessed at July 2016.

4. Olive, K. A. *et al.*, “Review of Particle Physics”, *Chin. Phys.*, Vol. C38, p. 090001, 2014.

5. Sauli, F., *Gaseous radiation detectors: fundamentals and applications*, Cambridge monographs on particle physics, nuclear physics and cosmology, Cambridge Univ. Press, Cambridge, 2014, https://cds.cern.ch/record/1645678, accessed at July 2016.

6. Mindur, B., “{ATLAS} Transition Radiation Tracker (TRT): Straw tubes for tracking and particle identification at the Large Hadron Collider”, *Nuclear Instruments and Methods in Physics Research Section A: Accelerators, Spectrometers, Detectors and Associated Equipment*, pp. –, 2016, http://www.sciencedirect.com/science/article/pii/S0168900216301905, accessed at July 2016.

7. The ATLAS TRT Collaboration, “The ATLAS Transition Radiation Tracker (TRT) proportional drift tube: design and performance”, *Journal of Instrumentation*, Vol. 3, No. 02, p. P02013, 2008, http://stacks.iop.org/1748-0221/3/i=02/a=P02013, accessed at July 2016.

8. The ATLAS TRT collaboration, “The ATLAS TRT electronics”, *Journal of Instrumentation*, Vol. 3, No. 06, p. P06007, 2008, `http://stacks.iop.org/1748-0221/3/i=06/a=P06007`, accessed at July 2016.

9. *Particle Identification Performance of the ATLAS Transition Radiation Tracker*, Tech. Rep. ATLAS-CONF-2011-128, CERN, Geneva, Sep 2011, `https://cds.cern.ch/record/1383793`, accessed at July 2016.

10. “TRT Test Beam Runs TWiki page”, `https://twiki.cern.ch/twiki/bin/view/Atlas/TrtTestBeamRuns?rev=16`, accessed at July 2016.

11. “TRT Test Beam Shifter Instructions TWiki page”, `https://twiki.cern.ch/twiki/bin/view/Atlas/TrtTestBeamShifterInstructions?rev=26`, accessed at July 2016.

12. “The Center for X-Ray optics:X-Ray Attenuation Length”, `http://henke.lbl.gov/optical_constants/atten2.html`, accessed at July 2016.

13. *ATLAS Inner Detector Alignment Performance with February 2015 Cosmic Rays Data*, Tech. Rep. ATL-PHYS-PUB-2015-009, CERN, Geneva, Apr 2015, `https://cds.cern.ch/record/2008724`, accessed at July 2016.

14. Frame, P. W., “A History of Radiation Detection Instrumentation”, *Health Physics*, Vol. 88, pp. 613–637, 2005, `http://journals.lww.com/health-physics/Fulltext/2005/06000/A_HISTORY_OF_RADIATION_DETECTION_INSTRUMENTATION.8.aspx`, accessed at July 2016.

15. Leo, W. R., *Techniques for nuclear and particle physics experiments: a how-to approach; 2nd ed.*, Springer, Berlin, 1994, `https://cds.cern.ch/record/302344`, accessed at July 2016.

16. Seltzer, S. M. and M. J. Berger, “Energy loss straggling of protons and mesons: Tabulation of the Vavilov distribution”, *Studies in penetration of charged particles*

in matter, Vol. 1, p. 187, National Academies, 1964.

17. Vavilov, P., "Ionization losses of high-energy heavy particles", *Soviet Phys. JETP*, Vol. 5, 1957.

18. Dolgoshein, B., "Transition radiation detectors", *Nuclear Instruments and Methods in Physics Research Section A: Accelerators, Spectrometers, Detectors and Associated Equipment*, Vol. 326, No. 3, pp. 434–469, 1993.

APPENDIX A: PLOTS FOR ARGON AND KRYPTON BASED MIXTURES

A.1. Argon

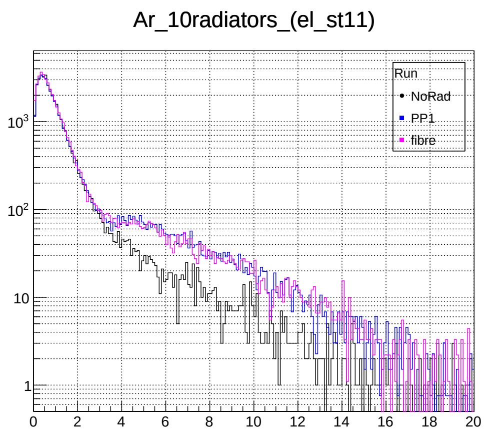

(a) Differential Spectrum

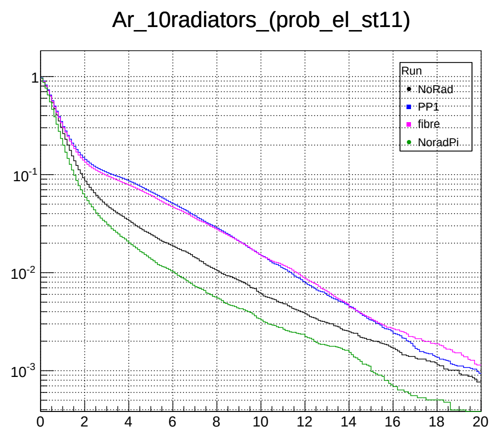

(b) Integral Spectrum

Figure A.1. Differential and Integral Spectrum Electrons, Straw 11, Argon

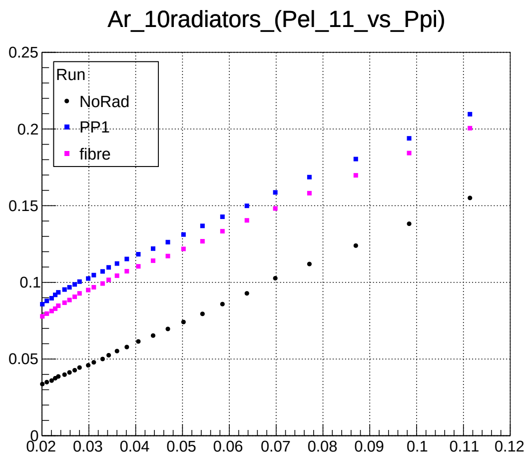

Figure A.2. Exceeding threshold probability, e^- vs π^-, Argon gas mixture.

A.2. Krypton

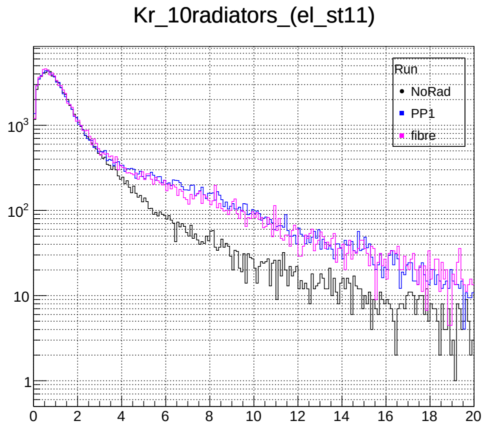

(a) Differential Spectrum

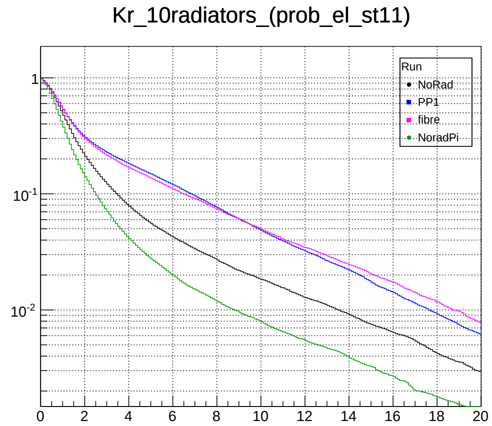

(b) Integral Spectrum

Figure A.3. Differential and Integral Spectrum Electrons, Straw 11, Krypton

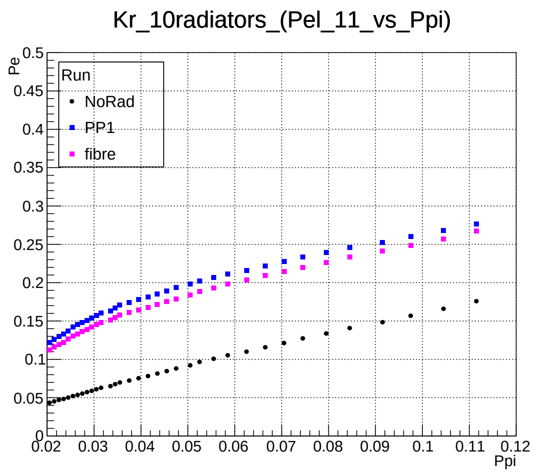

Figure A.4. Exceeding threshold probability, e^- vs π^-, Krypton gas mixture.